UCLA
UCLA Electronic Theses and Dissertations

Title
Multiband Polarimetric Imaging of Debris Disks with the Gemini Planet Imager

Permalink
https://escholarship.org/uc/item/9500f74t

Author
Arriaga, Pauline L

Publication Date
2020

Peer reviewed|Thesis/dissertation

eScholarship.org
Powered by the California Digital Library
University of California

UNIVERSITY OF CALIFORNIA
Los Angeles

Multiband Polarimetric Imaging of Debris Disks with the Gemini Planet Imager

A dissertation submitted in partial satisfaction
of the requirements for the degree
Doctor of Philosophy in Astronomy

by

Pauline Lim Arriaga

2020

© Copyright by
Pauline Lim Arriaga
2020

ABSTRACT OF THE DISSERTATION

Multiband Polarimetric Imaging of Debris Disks with the Gemini Planet Imager

by

Pauline Lim Arriaga
Doctor of Philosophy in Astronomy
University of California, Los Angeles, 2020
Professor Michael Fitzgerald, Chair

High-contrast imaging techniques have enhanced our capabilities in studying the formation and evolution of exo-solar disks and planets. In my research, I have studied the instrumentation, data reduction, and data analysis involved in this area. Many high-contrast imagers operate in the near-infrared wavelengths, the systems of which are rapidly developing with new technology. To this end, I have characterized the infrared detector of the upgraded Keck OSIRIS imager as well as explored methods for blocking out infrared radiation from the telescope components which pollute the desired scientific signal. Moving downstream from the data collection, I improved data reduction methods for suppressing the stellar signal from high-contrast images of disks and planets, as well as writing publically available code to forward model biases introduced from these subtraction methods. I generalized the code for these methods such that they can be used for most high-contrast imaging instruments, and optimized it for disks such that it ran two order of magnitudes faster than code optimized for planet detection. I studied the efficacy of my forward modeling module in further efforts to make the code more generally used by the scientific community. I used these techniques to study the debris disk HR4796A using multi-wavelength integral field polarimetric data form the Gemini Planet Imager (GPI). HR4796A hosts a well-studied debris disk with a long history due to its high fractional luminosity and favorable inclination lending itself well to both unresolved and resolved observations. We modelled a purely geometric disk in order to extract geometry parameters, polarized fraction and total intensity scattering phase functions for these data. We find that conventional methods that are used to model debris disks cannot produce a satisfactory model of the phase functions of the disk, indicating the need for more sophisticated grain models.

The dissertation of Pauline Lim Arriaga is approved.

Andrea Ghez

Ian McLean

Smadar Naoz

Michael Fitzgerald, Committee Chair

University of California, Los Angeles

2020

Посвящается Мише

TABLE OF CONTENTS

1 Introduction **1**

1.1 Debris Disks 2

1.2 Infrared instrumentation 4

1.3 Dissertation summary 4

2 Forward Modeling of Disks Using Karhunen-Loeve Image Processing . . **6**

2.1 Introduction 6

2.2 Data format 6

2.3 Karhunen-Loeve Image Processing 8

2.4 Forward Modeling and DiskFM 12

2.5 Forward modeling effects on generic disks 14

2.6 Varying brightness 14

2.7 Varying number of modes 15

3 Multiband Polarimetric Studies of the HR4796a Debris Disk **20**

3.1 Introduction 20

3.2 Data acquisition & processing 22

3.2.1 HR4796A observations 22

3.2.2 Data reduction 22

3.2.3 Polarized and angular differential imaging 22

3.2.4 Spectral mode observations 24

3.2.5 Convolution PSF construction 25

3.3 Prescriptive Modeling 26

3.3.1 Model description 26

3.3.2 Fitting procedure 28

3.4 Disk geometry results 29

3.4.1 Geometric parameters 29

3.4.2 Radial profile 37

3.5 Phase function 38

3.5.1 Phase curve extraction results 38

3.5.2 Dust grain modeling 41

3.5.3 Dust grain modeling results 42

3.5.4 Grain indices of refraction 47

3.5.5 Discussion 47

3.6 Conclusions 49

4 Instrumentation 50

4.1 Introduction 50

4.2 Pupil stops 51

4.2.1 Data 52

4.2.2 Model 52

4.2.3 Model fit 53

4.2.4 Pupil mask modeling 56

4.3 Hawaii2-RG detectors 56

4.3.1 Gain 59

4.3.2 Read noise 60

4.3.3 Dark current 62

4.3.4 Linearity 63

LIST OF FIGURES

2.1 Raw integral field polarimetric images. Green lines connect two lenslet images with orthogonal polarizations. Each red box represents a spaxel in the final polarization image. 7

2.2 Images of HR4796a at four different HWP angles orientations. The left panels are the total intensity images, or the sum of the polarized images, invariant to the position of the HWP. The right panels are the difference between two polarized images. Modulation of the HWP changes the axis of polarization. Combinations of four such images can be combined to form full Stokes' images. 8

2.3 The HR4796a total intensity in the K_1-band with no PSF subtraction (left) and post KLIP subtraction (right). 9

2.4 The zeroth (left) and fifth (right) KLIP basis vectors of the HR4796a covariance matrix. The large scale structure of the PSF is described by the zeroth basis vector while the smaller scale structure speckles are captured by the higher order basis vectors. 11

2.5 Example target image (left) and potential reference image (right). The exposures were taken 30 minutes apart, by which time the sky had rotated by an angle dθ, resulting in the disk image rotating the same dθ through the instrument speckle pattern. 11

2.6 The HD61005 debris disk with less aggressive (left) and more aggressive (right) PSF subtraction. The less aggressive subtraction only subtracts the zeroth basis vector, leaving PSF structure from wind and atmospheric effects. The more aggressive subtraction uses 10 basis vectors, resulting in a suppression of the PSF structure, but also in a significant loss of the disk's light. 12

2.7 A geometric model generated by an external code (left), a reduced data image of HR4796a (right) and the model image forward modeled using the basis vectors from the data image. 13

2.8 Results of the injection of brighter and dimmer HR4796a-like disks. The images in the lower panel are mock datasets in which a model-generated desk was injected into a GPI dataset. The lower middle pane images are the result of the KLIP reduction of the injected frames. The upper middle and left panels shows the best fit model to the KLIP dataset using forward modeling. The right panels show the residuals between the KLIP model and simulated data. 16

2.9 SPF of the input circular model disk inclined 70° and SPFs of walkers of the MCMC fits. 17

2.10 Results of the injection of brighter (upper) and dimmer (lower) edge-on disks. The images in the lower panel are mock datasets in which a model-generated desk was injected into a GPI dataset. The lower middle pane images are the result of the KLIP reduction of the injected frames. The upper middle and left panels shows the best fit model to the KLIP dataset using forward modeling. The right panels show the residuals between the KLIP model and simulated data. . 18

2.11 SPF of the input edge-on model disk shown in Figure 2.10 and SPFs of walkers of the MCMC fits. 19

3.1 Blue points indicate the locations of the spline points of the intensity of the disk around the disk. The number of spline points was determined to be the minimum number of points to recover a known SPF to a 1% level. The marked angles are the scattering angles assuming that the west side is closer to the observer. The extracted polarized phase function was cut off at a scattering angle of 120° where the disk signal falls below the noise level. The total intensity data was truncated at angles less than 20° and greater than 150°. 27

3.2 Injection and retrieval of a disk with a known Henyey-Greenstein model. 31

3.3 The left column shows the data, while the middle column shows the best fit model for the polarized intensity image. The right column shows the model subtracted from the data divided by the noise map. While most of the normalized residuals indicate per-pixel χ^2 under 1, the J-band image shows some structure. 32

3.4 Left column: KLIP PSF-subtracted J- and K_1-band data images. Middle left column: best-fit forward model. Middle right column: forward model subtracted from data divided by the noise map. Right column: convolved model before forward modeling. The shaded regions indicate areas we have omitted in our phase curve fits. Upper row: K_1band. Lower row: Jband. We chose not to fit to the Hband total intensity due to the small amount of field rotation. 33

3.5 Probability density distribution for the K_1-Pol parameters shown in Table 3.2. H-band and J-band polarized intensity show similar structure, though with wider distributions due to lower signal-to-noise. 34

3.6 Radial cuts of the data and model. Each of the data and model images were rotated such that the x-axis aligned with one of the radial locations marked in (d), which additionally shows the direction of the star center from the disk center with an exaggerated distance. A horizontal cut 4 pixels deep along the x axis were summed along the vertical axis. The solid lines show the cuts of the model images while the dashed lines are the cuts of the data images at each of the radial locations. 36

3.7 Model led polarized intensity phase curves as a function of scattering angle. The data points show the locations of the fitted spline points. The 3-σ data point error bars are overlaid, but are smaller than or equal to the size of the points. The shaded regions represent the 3-σ range of the phase curve, derived from the scatter of the splines generated from each MCMC walker's spline point values. The curves are truncated at 120° where the signal is dominated by the noise. . 39

3.8 Upper panel: K_1-band polarized intensity phase curves. Lower panel: K_1-band total intensity phase curves. These curves are normalized at 13° and the error bars are derived from the scatter of the MCMC walkers' splines. The shaded portions at 20° and 140° were excluded from analysis where the signal to noise is low due to attenuation by the PSF subtraction. The data points indicate the locations of the curve spline points. Lower panel: K_1-band polarized fraction. The polarized fraction is derived by dividing the unnormalized polarized intensity phase curve from the unnormalized total intensity phase curve. The south-west curves are plotted in blue, while the north-east curves are plotted in red. 40

3.9 MCFOST fits of the K_1-band total intensity (upper) and polarized fraction (lower). The data-extracted curves and associated errors are shown in blue, while the red shows the best-fit curve for DHS and the green shows the best-fit curve for Mie. 44

3.10 Best fit total intensity phase curves fitting only to K_1-band total intensity data for Mie theory (left) and DHS (right). 45

3.11 Best fit polarized fraction phase curves to only the K_1-band polarized fraction for Mie (left) and DHS (right). 45

3.12 Marginalized probability maps of the DHS (upper) and (Mie) models for total intensity (left) and polarized fraction(right), gained by summing along the probability matrix along the $a_{\min}$ and $a_{\exp}$ axes. Overplotted are indices of refraction of representative dust grains (Khare et al., 1984; Pollack et al., 1994; Zubko et al., 1996; Li & Greenberg, 1997, 1998; Li & Draine, 2001) 48

4.1 Top-down picture of the new OSIRIS imager. The light path is indicated by the blue arrows. The relay of the off-axis parabolic mirrors (indicated in orange) achieves a field of view of 19″×19″. The design also allows for a well-formed pupil, allowing for matched pupil masks to be installed in the filter wheels (pictured in red). Finally, the new Hawaii-2RG detector is indicated in green. 51

4.2 Mosiaic of the six images images taken in Kp band (left) and model fit (right) . 53

4.3 Components in the plane of the secondary mirror. The secondary support holds the secondary mirror scaffold shown in light green. In front of this scaffold are the baffle tube in purple, other secondary mirror scaffolding and the secondary mirror itself which are completely opaque to the emission of the secondary obscuration. 54

4.4 Image fits of Br-α (4.1μm) and Kp (2.1μm). The uniform background is much more prominent in Kp, while the thermal emission is more dominant in Br-α . 55

4.5 The relative signal to noise for Kp band (thicker blue lines) and Br-α (thinner green lines) with hexagonal masks (dashed lines) and annular masks (solid lines). The radii shown are in units of meters in the primary plane. 57

4.6 The best fit inner masks for Kp in green and outer masks in blue. 57

4.7 Reference radius locations for measurements listed in Table 4.2 58

4.8 The median of the median and variance maps at each lamp brightness. The inverse of the slope of the fitted line implies a gain of 2.16 ± 0.34. 60

4.9 Median counts as a function of integration time with a constant lamp brightness. A linear fit to the lower data points is shown in blue while a parabolic fit to the upper data points is shown in red. 62

4.10 Electrons as a function of time in a dark setting. This implies an upper limit on the dark current of $<.021$ e^{-}/pix/s 63

LIST OF TABLES

3.1 Observations 23

3.2 Notes. We chose to fit the PA and inclination separately for each disk in order to account for uncertainty in rotation of the instrument relative to north due to the instrument being in different cycles, as well as differences due to flexure. Furthermore, we fit the radial profile parameters to account for possible differences in the structure of the disk of different grain sizes. The fifth column lists the parameters found, averaged over the H, H2, and H3 bands, by Milli et al. (2017), and the sixth lists the average parameters found by Schneider et al. (2014) with the F25ND3 filter. The radius for Milli et al. (2017) is the average distance from the star of points along an ellipse with a semimajor axis $a = 1.066$" and an ellipticity $e = 0.07$. 30

3.3 Note: The real and imaginary indices of refraction were chosen to reflect limits seen in physical grain models at the central wavelength of $2.15\mu m$ 42

3.4 Best fit parameters for different χ^2_ν for different grain models. The bolded column indicates the χ^2_ν each set of parameters was optimized for. The third column shows the sum of the total intensity and polarized fraction χ^2_νs. The fourth column and fifth columns are the χ^2_ν values for the total and polarized fraction, respectively. The second column describes the metric over which the best fit parameters were derived. The second and fifth rows list the best fit parameters in the sixth to ninth columns for the best summed χ^2_ν. The third and sixth columns are the parameters for the best total intensity χ^2_ν and the fourth and sixth list the best fit parameters for the best polarized intensity. 46

4.1 Dimensions of components in meters. 55

4.2 Radii of inner and outer portions of the masks. 58

4.3 Read noise for varying numbers of reads and integration times for MCDS exposures. 61

4.4 Linearity characteristics 61

ACKNOWLEDGMENTS

On the day I was born, one of six total eclipses of the decade occured. A more superstitious person might have seen this as an auspicious omen of success in my future studies of astrophysics. Though I do not put any stock in fate, I know that I have been incredibly lucky to have had people in my life who have shaped who I am and supported me along the way. First and foremost, I am eternally grateful to my parents, who have always encouraged my curiosity in all aspects of knowledge and imparted me with an invaluable work ethic, which has compensated for the many skills in which I lack any "natural talent." They ensured that I went to San Diego High School, one of the best public high schools in the country, where I was able to study under excellent teachers who have prepared me to face the most difficult of academic challenges. I would especially like to thank David Evers who taught me not only physics, but also how to teach students of my own. By more even more luck, I decided to go to UC Berkeley despite not knowing much about the phenomenal education I would receive from the physics, astronomy, and Russian departments.

I am eternally grateful to my first research advisor, Gaspard Duchêne, who first sparked my interest in studying debris disks and exoplanets, and who has continued to mentor me over the past ten years. Of course, I have to thank my graduate school advisor Mike Fitzgerald, who has provided me with guidance and support for much of the research presented here. He has truly allowed me to be an independent researcher, even though it has resulted in me being a general nuisance wandering through an endless long train of rabbit holes. On top of the fantastic advisors under whom I have studied, I would not have accomplished so much without the help of every member of the entire Gemini Planet Imager team, especially Christine Chen, Jason Wang, Max Millar-Blanchaer, Rahul Patel, and Johan Mazoyer, who have made significant contributions to this work and others.

Equally as important as my academic supporters to any success I have had are those who have provided endless moral support. For more than twelve years, my friends Paquita Esterly, Antonio Soto, and Michael Markson have helped me through every step of the way. I have to thank my co-habitants in the Berkeley astronomy lab with whom I shared an unhealthy number of sleepless nights, especially Jhett Bordwell, who has seen me through the good and bad during those four years of undergraduate school. I also have to thank my friends who have helped me navigate the uncertain world of graduate school, especially the women of the IR lab, Emily Martin, Sara Logsdon, and Anna Boehle. I thank all of the members of Mariachi de Uclatlán who have provided me a musical outlet to keep me sane, especially Julio Rodriguez, and Chuy Guzmán for six years of music tutelage.

Finally, I have to thank my boyfriend Misha, whose Russian class was the perfect escape for the stresses of the first two years of graduate school. The following four years of companionship, love, morning cups of coffee, and walks on the beach have brought so much happiness through the most stressful times of life.

This research is funded in part by the Gordon and Betty Moore foundation through Grant GBMF3847 to UCLA and NSF AST-1413718 and AST-1615272, NASA AST-NNX15AC89G, NASA AST-1413718, NASA AST-1615272.

VITA

2016-2020	UCLA, Los Angeles, California Graduate student researcher
2016	UCLA, Los Angeles, California M.S. in Physics
2014	University of California - Berkeley, Berkeley, CA B.A in Physics, B.A in Astronomy

PUBLICATIONS AND PATENTS

P. Arriaga, Modeling the transmission and thermal emission in a pupil image behind the Keck II adaptive optics system *SPIE*, 2016

P.Arriaga, M. P. Fitzgerald, Upgrade and Characterization of the OSIRIS Imager Detector *SPIE*, 2018

P.Arriaga, M. P. Fitzgerald, Multiband Polarimetric Imaging of HR 4796A with the Gemini Planet Imager, *apj*, sub

J. Mazoyer, P. Arriaga, Forward Modelling Techniques for Spectra Retrieval of Circumstellar Debris Disks, *spie*, 2018

J. Mazoyer, P. Arriaga, DiskFM: A Forward Modeling Tool for Disk Analysis with Coronagraphic Instruments, *spie*, in prep

CHAPTER 1

Introduction

Records of the movements and evolution of celestial bodies span the entirety of human history. Various cultures have interpreted the changing positions of the stars, moons, and planets in different ways: for some, the North Star has been a trusted guide through journeys by land or sea; for others, the yearly rising and setting of the Pleiades mark the seasons for harvesting and planting new crops. What early man conceived as the divine "trepidation of the spheres"[1] is now properly understood as the consequences of the laws of physics. This shift from the phenomenological to the scientific has been possible solely due to advancements in mathematics and technology. Improvements in optics and light detectors yield greater capabilities in the collection of data on stars and planets. Advancements in mathematics have enabled us to better interpret an ever-growing accumulation of data. In the contemporary field of astrophysics, these developments have emerged as three main modes of study: instrumentation, data reduction, and theory. In my own research, I have aspired to work on projects in each of these three aspects, to follow the entirety of the arc from signal to theory. My focus has been the study of exosolar systems in infrared light to answer fundamental questions about the formation and evolution of planetary systems. In my instrumentation work, I researched the properties of the detector, which translates infrared light to raw data images. In my data analysis work, I helped develop a pipeline that renders raw images into processed data ready for interpretation. In my theoretical work, I then analyzed this reduced data to further our understanding about the exosolar systems.

---

[1] The Valediction Forbidden Morning by John Donne

1.1 Debris Disks

Since the discovery of the first exoplanets nearly 25 years ago (Mayor & Queloz, 1995), the field of studying exosolar systems has developed rapidly in an attempt to answer fundamental questions about the formation and evolution of planetary systems. As the technological capabilities of astronomical facilities have improved, so has our understanding of the characteristics of these systems, revealing a wide diversity of the planets, their formation, and the dynamics governing their configurations. Each of the ever-growing number of detection and characterization techniques provides a unique wealth of knowledge for understanding the ever-growing number of discovered planets.

With the advent of large telescopes with advanced wavefront control techniques, it has become possible to directly image exoplanets (Macintosh et al., 2006; Beuzit et al., 2019). Whereas transit and RV techniques for characterizing exoplanets favor large planets at close star-planet separations, direct imaging techniques aim to detect planets at a closer analogue to the gas giants of our own solar system. Direct imaging surveys have shown that the occurrence rate of planets with a brightness and star separation that can be currently be detected by direct imaging methods is fairly small (Bowler & Nielsen, 2018), requiring careful choices in targets to observe. Instrumental in discovering some directly imaged exoplanets, such as β- Pictoris b (Lagrange et al., 2010) and Fomalhaut b (Quillen, 2006a), has been analysis of their debris disks.

Debris disks are a class of evolved circumstellar disks, analogous to the zodiacal light and Kuiper belt of our solar system. The distinguishing feature of debris disks from protoplanetary disks is that the dust and gas components are not primordial, rather, is continually replenished by collisions between protoplanets (Wyatt, 2008). Observationally, debris disks are identified by low optical depths and relatively low levels of gas. Hundreds of debris disks were discovered photometrically by detection of far-infrared excess originating from the thermal emission of the dust grains (Chen et al., 2014). Resolved images of dust-scattered light have provided a different approach to understanding exosolar systems. The observed image is the outcome of both the surface density and composition of the dust, both of which lend well to drawing analogies between our debris disks and those of other planetary systems and studying trends in other planetary systems. Physical features such as sharp radial profiles, warps, clumps and spirals can be interpreted as effects of unseen planets or interactions with the interstellar medium (Nesvold & Kuchner, 2015; Quillen, 2006b; Olofsson et al., 2019). However, any modeling of the physics of the systems requires knowledge or accounting of properties of the individual dust grains.

The composition, size relative to the wavelength of the observation, and shape of the dust grain determine the amount of light scattered as a function of the scattering angle (the angle between the incoming and outgoing rays of light, such that forward scattering occurs at 0° and backwards scattering occurs at 180°). A larger dust grain, for example, is more forward scattering, meaning that light is preferentially scattered at small scattering angles (Bohren & Huffman, 2009). Conversely, smaller dust grains efficiently scatter at all scattering angles. The indices of refraction of the dust grain additionally affects the efficiency of the dust grain scattering. The overall scattering efficiency of an ensemble of dust grains as a function of phase angle is called the scattering phase function (SPF). In addition, a calculated SPF can differ considerably with different theories of the light scattering. In modeling debris disks, using Mie theory to calculate the SPF, assuming porous spherical particles, has been favored due to its relatively fast calculation. Mie theory has been able to generate good fitting models in most debris disk (Hughes et al., 2018, and references therein), with the notable exception of the disk HR4796A, which is the focus of Chapter 3. Dust particles collected from the 67P/Churyumov-Gerasimenko comet, which also exhibits a similarly unusual function, have been shown to be aggregate particles (Mannel et al., 2016). Calculating scattering phase functions for aggregate particles is considerably more computationally expensive and scales exponentially with particle size, and so calculating the phase function for a distribution of hollow spheres (Min et al., 2005, DHS) has served as a proxy. However, this analogy is empirical, and is untested for larger grain sizes. In Chapter 3, we test the validity of this approximation by attempting to fit a DHS SPF model to the anomalous HR4796A. We measure not only the SPF for HR4796A but also the polarized SPF extracted from polarimetry data from the Gemini Planet Imager (GPI), a high-contrast imaging operating at the Gemini South Telescope.

Though the ratio between the brightness of the HR4796A disk to the star in infrared wavelengths is fairly high (Jura, 1991, $f = L_{IR}/L_* = 5 \times 10^{-3}$)), accessing the maximal amount of the SPF requires sophisticated subtraction of the star's point spread function (PSF). Due to atmospheric effects, the PSF is dynamic, varying from frame to frame, requiring an equally dynamic PSF subtraction algorithm. One such algorithm is the Karhunen-Love Image Processing (KLIP) algorithm, which is detailed in Chapter 2.

1.2 Infrared instrumentation

The OSIRIS (OH-Suppressing Infra-Red Imaging Spectrograph; Larkin et al. 2006) is an instrument with an integral field spectrograph and imager mode operating in infrared wavelengths. OSIRIS has undergone an upgrade, replacing the imager that included a new infrared detector. We performed characterization tests on the new Teledyne Hawaii-2RG (H2-RG) detector. We determined the gain, the read noise, dark current, and linearity characteristics.

Another component of the upgrade was the manufacture of new pupil stops, which aim to block thermal emission from different elements of the telescope. To optimally block thermal emission from the Keck II telescope elements, I modeled the pupil based on images from the NIRC2 pupil imaging mode. I then calculated the optimal the size and geometry of different pupil masks, which contributed to the final design of the physical masks.

1.3 Dissertation summary

In Chapter 2, I describe my contributions to a module of a point spread function (PSF) subtraction algorithm, PyKLIP (Wang et al., 2015), which is used for forward modeling extended objects such as disks.

In Chapter **??**, I present the results of a study of the HR4796A debris, in which I analyze the physical morphology of the disk and models of its unusual SPF.

In Chapter 4, I report on instrumentation work modeling the Keck II pupil and the characterization of Hawaii-2RG detectors.

CHAPTER 2

Forward Modeling of Disks Using Karhunen-Loeve Image Processing

2.1 Introduction

The Gemini Planet Imager (GPI) is a high contrast imaging instrument on the Gemini South telescope which was built to directly image planets and disks (Macintosh et al., 2006; Beuzit et al., 2019). In order to achieve the contrast (ratio of the brightness of the target and the star) needed to detect disks and planets, GPI employs an extreme adaptive optics (AO) system and a coronagraph. Both of these components, among other optics, result in a dynamic and complicated stellar point spread function (PSF) in the reduced frames. Due to this instability, the stellar PSF subtraction required to detect disks and planets, similarly needs to be dynamic. Much of GPI data is PSF subtracted using the Karhunen-Loeve Image Processing (KLIP). In this chapter, I discuss the effects of the Karhunen-Loeve Image Processing algorithm in the context of disks. I additionally discuss the DiskFM module that I wrote for the Python implementation of KLIP (Wang et al., 2015) PyKLIP, as well as the optimal parameters for various use cases.

2.2 Data format

In GPI's integral field polarimetric mode, light passes through a lenslet array which samples the light in the pupil plane. The beam from each lenslet passes then through a polarizing beam splitter creating two distinct for each lenslet at orthogonal polarizations. An example raw image are Figure 2.1, where pairs of lenslet spots are connected by green lines. The upper

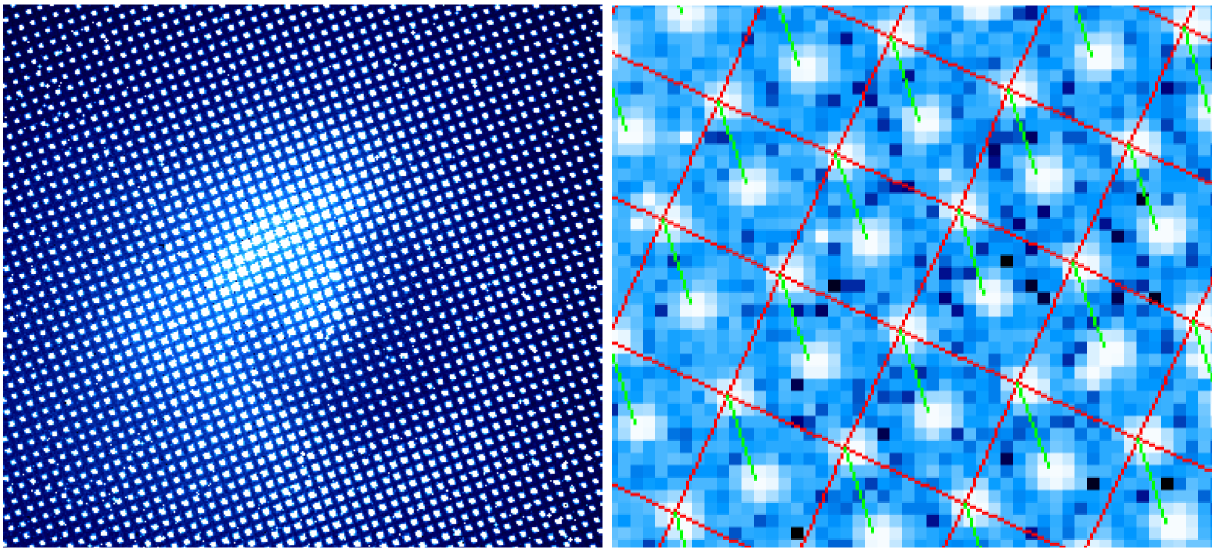
(a) (b)

Figure 2.1: Raw integral field polarimetric images. Green lines connect two lenslet images with orthogonal polarizations. Each red box represents a spaxel in the final polarization image.

and lower spots are extracted into two separate polarized images. The light is modulated between each exposure using a half-wave plate (HWP) which rotates between four different positions. The right panels of Figure 2.2 show the difference of the orthogonal polarized images at the four HWP positions positions. A combination of difference images at the four positions of the half wave plate can be combined to form the four Stokes' components (I, Q, U, V) using an algorithm described in Perrin et al. (2015).

The I component, containing the total amount of light passing through the system, is gained by summing the orthogonal polarized images, examples of which are shown in the left panels of Figure 2.2. Herein and throughout this this work, I will refer to intensity the Q vector images as the polarized intensity and the intensity of the I in image as the total intensity. As both the total intensity and polarized intensity are extracted the same image there is no calibration required to compare the two, which is fortuitous as the calibration factor between ADU and absolute flux units in GPI images has proved to be unreliable as images from night to night (Chen et al, sub). Therefore, the main quantity that will

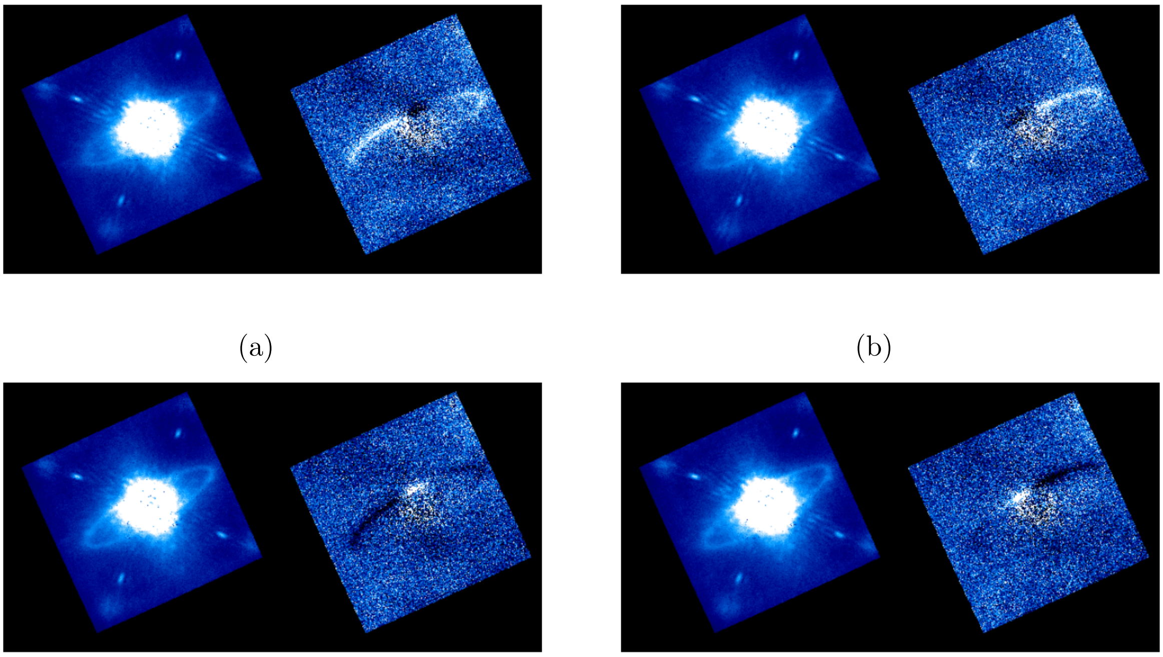

(a) (b)

(c) (d)

Figure 2.2: Images of HR4796A at four different HWP angles orientations. The left panels are the total intensity images, or the sum of the polarized images, invariant to the position of the HWP. The right panels are the difference between two polarized images. Modulation of the HWP changes the axis of polarization. Combinations of four such images can be combined to form full Stokes' images.

be studied is the polarization fraction, the unitless ratio between the polarized and total intensity. However, in order to find the total intensity of the disk, the stellar PSF needs to be subtracted to extract the disk flux. The complex structure of the PSF in the final image of HR4796A is shown in Figure 2.3,

2.3 Karhunen-Loeve Image Processing

In order to subtract model stellar PSF, we employed the KLIP algorithm. The first step of the process is to the calculate the covariance matrix of a set of reference images (Soummer et al., 2012). The eigenvectors of the covariance matrix forms a basis set of images. Analogous to

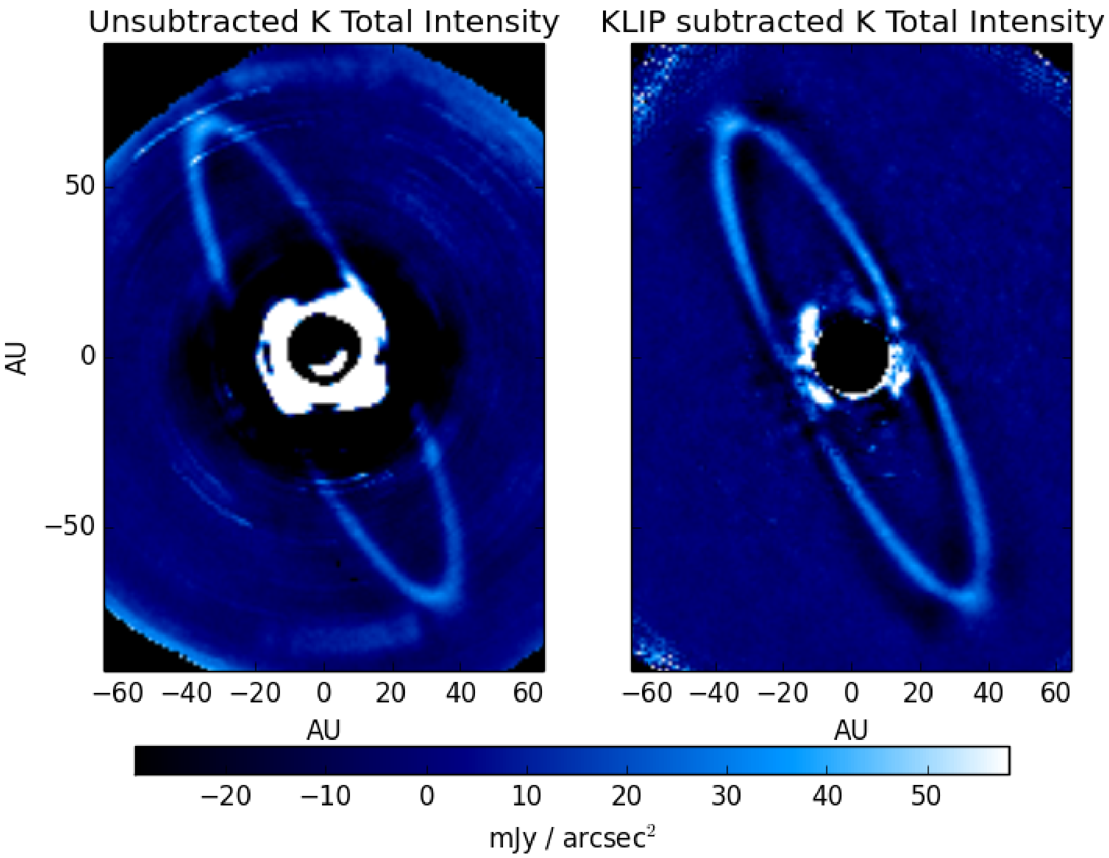
Unsubtracted K Total Intensity
KLIP subtracted K Total Intensity
50
0
−50
AU
−60 −40 −20 0 20 40 60
AU
−60 −40 −20 0 20 40 60
AU
−20 −10 0 10 20 30 40 50
mJy / arcsec²

Figure 2.3: The HR4796A total intensity in the K_1-band with no PSF subtraction (left) and post KLIP subtraction (right).

sinusoids and periodic signals in Fourier transforms, any GPI stellar PSF can be constructed from an infinite linear combination of these basis vectors. Examples of basis images are shown in Figure 2.4. The lowest order basis vector captures the largest scale structure, whereas the higher order basis vectors captures some of the smaller scale speckle noise. Projecting each target exposure onto the basis set produces a model of the star's PSF. Subtracting this PSF model from the target image should only leave the disk or planet image. A final combination of the subtracted images is shown in Figure 2.3.

In a perfect system, the covariance matrix would be formed from an infinite reference library. It is necessary to carefully choose reference images that are as close to the same conditions of the target exposures for computational efficiency.

The angular differential imaging method (ADI), takes advantage of the fact that GPI is a pupil tracking instrument and so the disk/planet signal rotates through the PSF structure over the course of the night. This effect is exemplified in Figure 2.5 which shows raw total intensity exposures taken 30 minutes apart. Due to the sky rotation disk rotates an angle dθ with respect to the four satellite spots which are intentionally scattered by instrument optics to provide positional reference. A target image can then use any exposures in the same sequence as long as the $\Delta\theta$ is sufficiently large that the disk in the reference image does not overlap with the astrophysical signal in the target image. The advantage of using ADI is that the reference images share conditions such as stellar spectrum, wind speed, weather, and seeing, the target image, though the exact structure of the PSF varies with fidelity of the adaptive correction. The minimum rotation needed for an exposure to be used as a reference image for a target exposure is a tuneable parameter in the implementation of ADI in PyKLIP. The minimum rotation is tuned to reduce an effect of the KLIP algorithm called self-subtraction. Self-subtraction arises from the presence of the disk in the reference images, which influences the basis vectors. Increasing the minimum rotation reduces the intersection between the disk in the reference image and target image. However, increasing the minimum rotation decreases the number of reference images which may lead to a worse model of the PSF. For a disk which has a high inclination like HD 61005 shown Figure 2.6, the minimum rotation can be relatively small, while a lower inclination such as HR4796A shown in Figure 2.3 requires a larger minimum rotation.

Another important consideration in reducing disk data is the number of basis vectors to subtract. The largest scale structure is modeled by the lowest basis vectors as shown in Figure 2.4, while the smaller speckles must be modeled by combinations of higher order basis vectors. While using more basis vectors creates a better PSF model, it also causes more the disk structure to be lost. As an example, Figure 2.6 shows two different reductions of the total intensity image of the HD61005 disk. Only one basis vector is used on the left image, while 10 are used in the image on the right. While there is a clear detection of the backside in the less aggressive PSF subtraction, the flux is indistinguishable from the PSF structure in many places. In the more aggressive subtraction, the backside of the disk is undetected

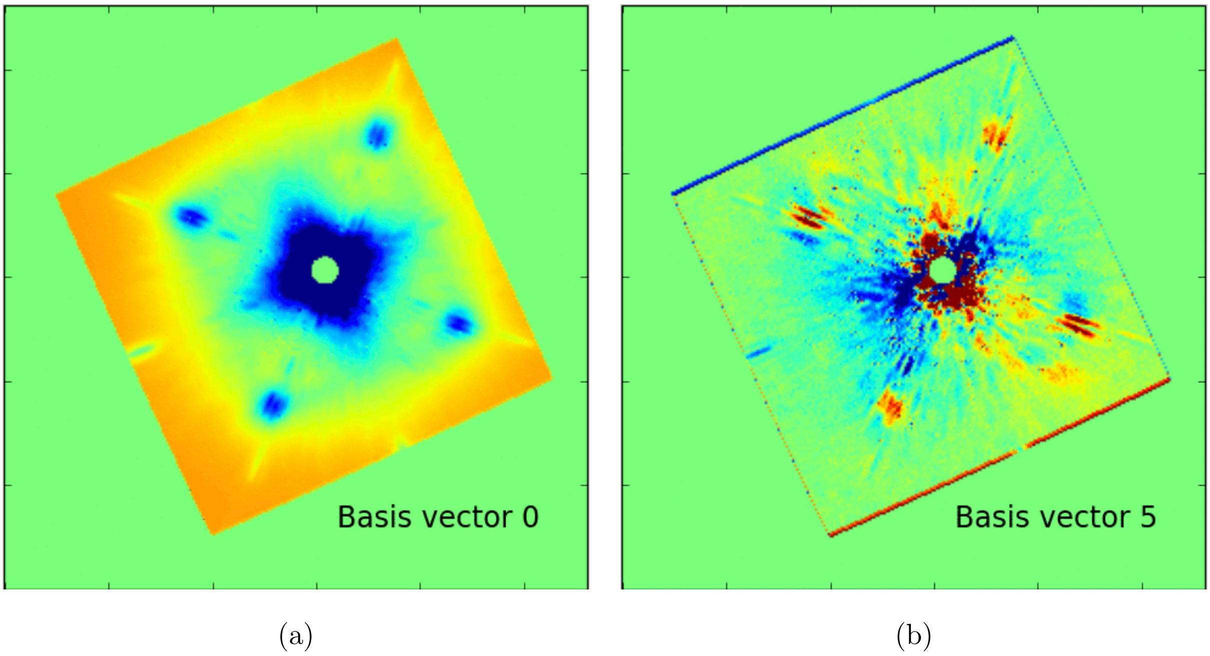
Basis vector 0
Basis vector 5

(a) (b)

Figure 2.4: The zeroth (left) and fifth (right) KLIP basis vectors of the HR4796A covariance matrix. The large scale structure of the PSF is described by the zeroth basis vector while the smaller scale structure speckles are captured by the higher order basis vectors.

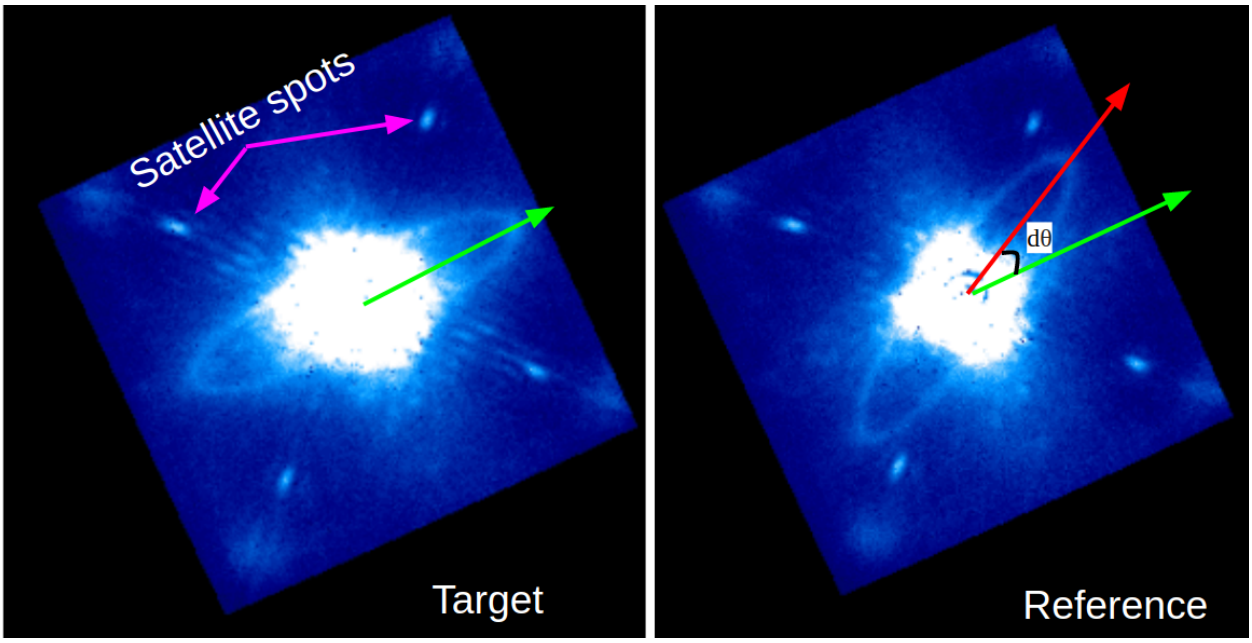
Satellite spots
Target
dθ
Reference

Figure 2.5: Example target image (left) and potential reference image (right). The exposures were taken 30 minutes apart, by which time the sky had rotated by an angle dθ, resulting in the disk image rotating the same dθ through the instrument speckle pattern.

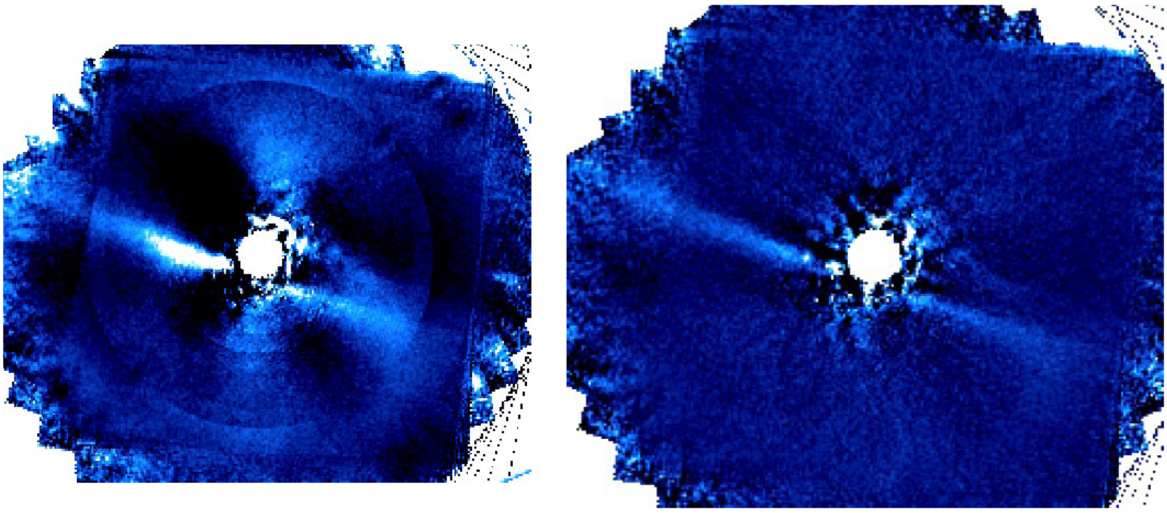

Figure 2.6: The HD61005 debris disk with less aggressive (left) and more aggressive (right) PSF subtraction. The less aggressive subtraction only subtracts the zeroth basis vector, leaving PSF structure from wind and atmospheric effects. The more aggressive subtraction uses 10 basis vectors, resulting in a suppression of the PSF structure, but also in a significant loss of the disk's light.

though the midplane of the disk is more defined, and the distinction between the speckles and disk is much clearer. This loss of flux by increasingly aggressive subtractions is called over-subtraction.

2.4 Forward Modeling and DiskFM

A more unbiased determination of the brightness and geometry of astrophysical signals without the artifacts self-subtraction and over-subtraction requires modeling of the behavior of KLIP. To this end, we implemented a forward modeling routine, DiskFM, based on Pueyo (2016) which reconstructs the ADI/KLIP processed image, accounting for the impact of the disk image on the formation of the KL basis. An example of a forward model is shown in Figure 2.7, with the model image, as well as the model which had been forward modeled using the basis vectors of the shown data image. Pueyo (2016) studied the efficacy of KLIP forward modeling on point sources, but deferred studies of KLIP-FM on disks noting that

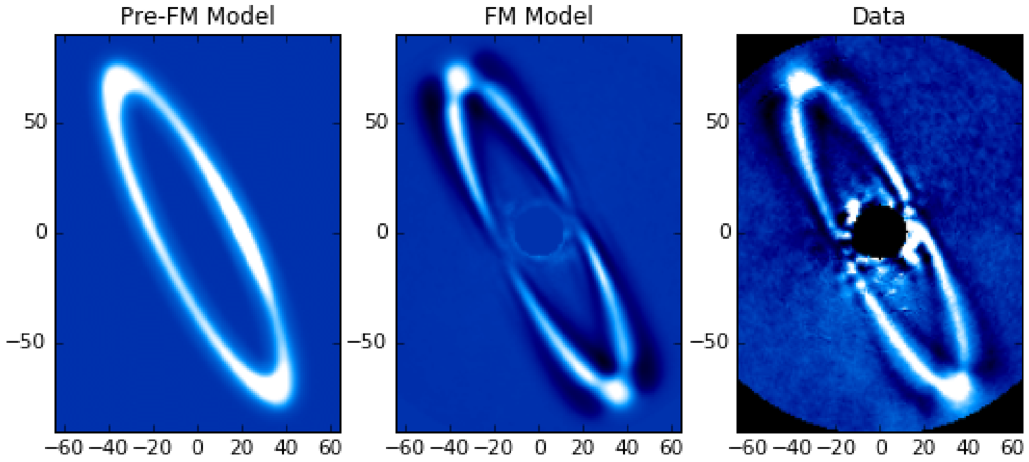

Figure 2.7: A geometric model generated by an external code (left), a reduced data image of HR4796A (right) and the model image forward modeled using the basis vectors from the data image.

the problem "cannot be simplified using a simple PSF as the astrophysical model: every hypothetical disk morphology must be explored". DiskFM is intended to be used with a fitting algorithm which may generate models of the disk scattered-light image. As such, the algorithm cannot be memory intensive and must be as efficient as possible in a multi-threaded framework.

The initial step of DiskFM is to perform KLIP on the data images, saving the basis vectors as well as the reduced image into a HDF5 file. This step is the most intense part of the calculation, but only needs to be done once. Once the basis vectors are saved, they do not need to be calculated again unless the minimum rotation or the reduction zones are changed. The save file is generalized such that it can be read into any Python 3+ session and does not even have to be recalculated even when transferred to different servers or computers. When initializing a fitting algorithm, the reduced image and basis vectors are first loaded into the session. Then, during the fitting steps, models with varying geometric parameters and SPFs are generated using external codes and forward modeled using DiskFM. The forward modeled image can then be compared to the reduced image as an iterative step in the overall fitting process.

2.5 Forward modeling effects on generic disks

In Section 2.3, we described the parameters used to tune for optimization in reducing the data. Optimization of these parameters for the PSF subtraction is relatively straightforward to do on a case-to-case basis, by measuring the signal to noise (S/N) at various points along the disk. However, the number of basis vectors to use for KLIP-FM in a fitting algorithm is much less straightforward for reasons that will soon become apparent. Here, we will attempt to study the effects of using different KLIP parameters to fit two types of disks: an inclined disk similar to HR4796A, and an edge-on disk, similar to HD32297. More extensive studies will be discussed in Mazoyer et al 2020, in prep. We will test the efficacy of different KLIP parameters using DiskFM by generating mock datasets by injecting model disks GPI datasets with no detected disks. We will then attempt to retrieve the geometric and SPF parameters by fitting forward modeled disks using an Markov chain Monte Carlo (MCMC).

2.6 Varying brightness

The case of an inclined disk is simplest case for using ADI and extracting a phase function. Figure 2.8 shows disks with Henyey-Greenstein parameters generating a SPF similar that of HR4796A. We generated a bright (high S/N) and dim (low S/N) version of the disk, and injected each into an empty dataset to create simulated data. We then used an MCMC fitter to generate models of varying SPF parameters. The best fits are shown in Figure 2.8. Visually, the fitter performed well for both the dim and bright disks, with almost no residuals in the final image. Differences in performance are more apparent in the the phase functions generated by the final MCMC walkers, shown in Figure 2.9. Both fitters can reproduce the injected curve, though the brighter disk has tighter constraints on the parameters.

2.7 Varying number of modes

Determining the SPF for an edge-on is an important problem since highly inclined disks are preferentially detected (Esposito et al., 2020). Figure 2.10 shows the models we generated with similar SPF and geometry parameters to HD32297. The backside of the disk is barely resolved in the unconvolved model, and completely unresolved in the convolved image. Furthermore, ADI tends to attenuate flux in the vertical direction relative to the midplane, making any determination of the backside SPF even more difficult. As will be shown in Chapter 3, the full SPF is crucial for making determinations of the dust properties. In the test demonstrated in Figure 2.10, we modeled the same mock dataset, but with using one 3 basis vectors in the forward model and 20 in another. The mock data reduction of the image using only 3 KL basis vectors exhibits a large butterfly-shaped structure in the background. This effect is mostly suppressed in the reduced image using 20 KL basis vectors. However, the residuals in this fit exhibit strong, and sharp structure around the midplane of the disk because of the self-subtraction.

Figure 2.11 shows the resulting phase curves of the fits. While both can recover the phase curve on the front side fairly well, only the reduction using 20 basis vectors can recover the phase curve of the back side. This test shows the unpredictability of fitting using forward modeling in extreme cases. In a situation with real data with an unknown phase function, we would have been unable to determine whether or not the back side of the disk was correctly recovered. The SNR residuals are comparable enough that one may elect to use the less computationally expensive reduction which uses only 3 KL basis vectors. On the other hand, in the case of a bright slightly inclined disk such as HR4796A, it is safe to use fewer basis vectors, as will be shown in Chapter 3. Because of this, in future work, we aim to complete these tests on a wider range of mock disks to inform optimal parameters to use when fitting for specific disk geometries.

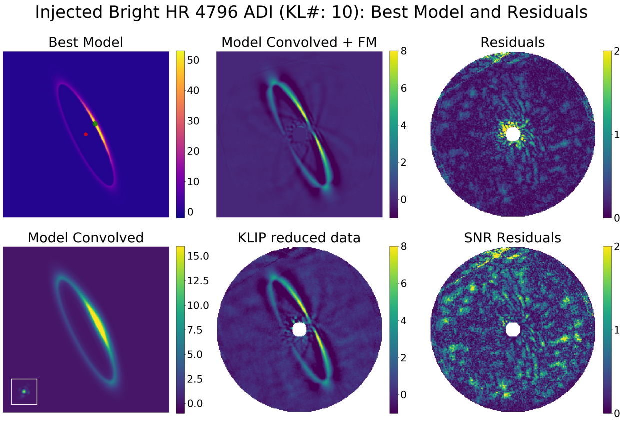

(a) Injection and retrieval of a bright disk.

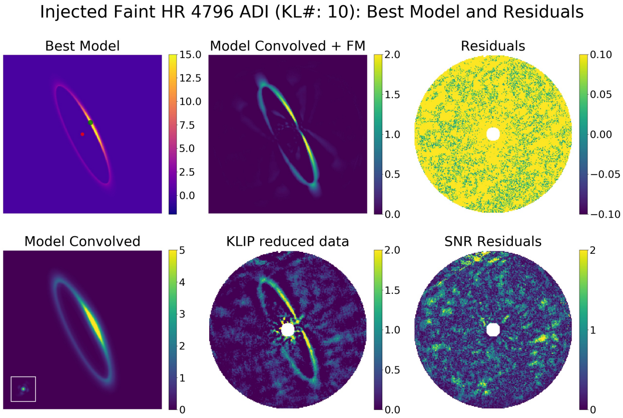

(b) Injection and retrieval of a dimmer disk.

Figure 2.8: Results of the injection of brighter and dimmer HR4796A-like disks. The images in the lower panel are mock datasets in which a model-generated desk was injected into a GPI dataset. The lower middle pane images are the result of the KLIP reduction of the injected frames. The upper middle and left panels shows the best fit model to the KLIP dataset using forward modeling. The right panels show the residuals between the KLIP model and simulated data.

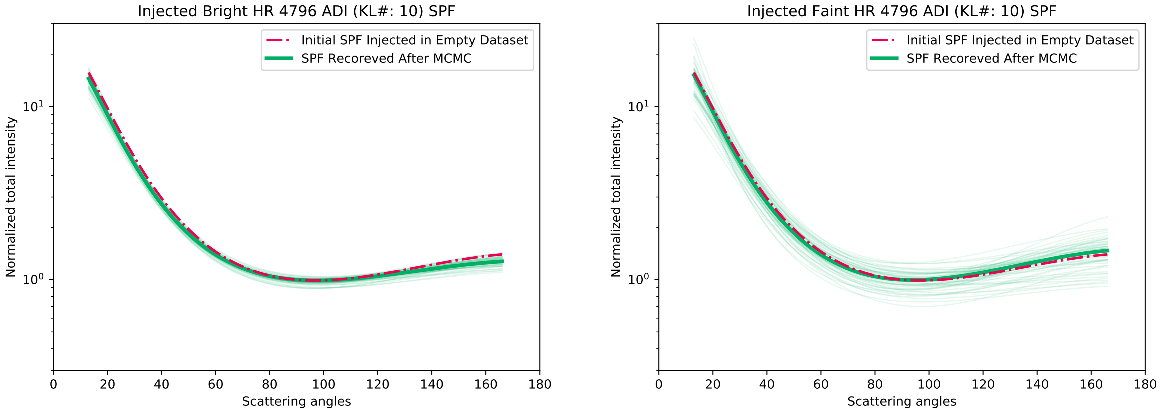

(a) Injected and retrieved SPF of brighter disk (b) Injected and retrieved SPF of dimmer disk

Figure 2.9: SPF of the input circular model disk inclined 70° and SPFs of walkers of the MCMC fits.

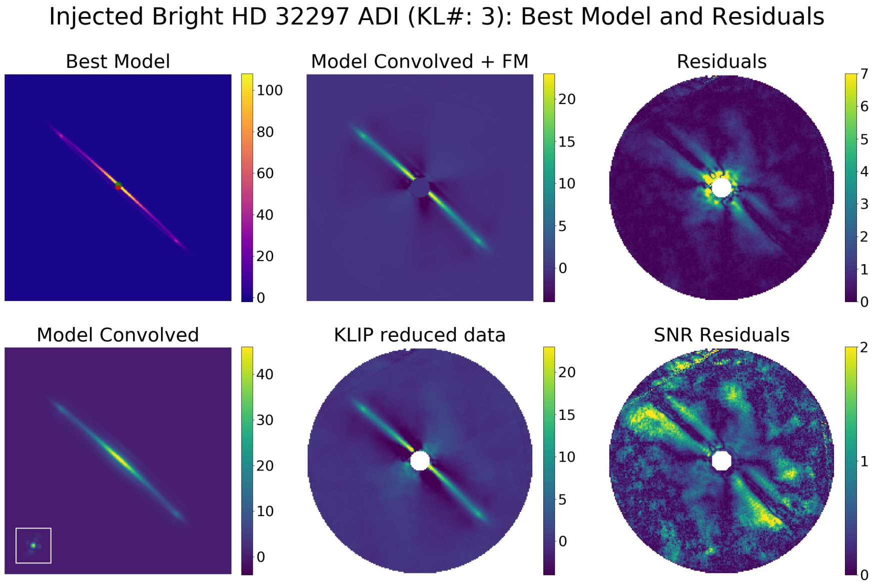

(a) Fits to mock data using 3 KL basis vectors

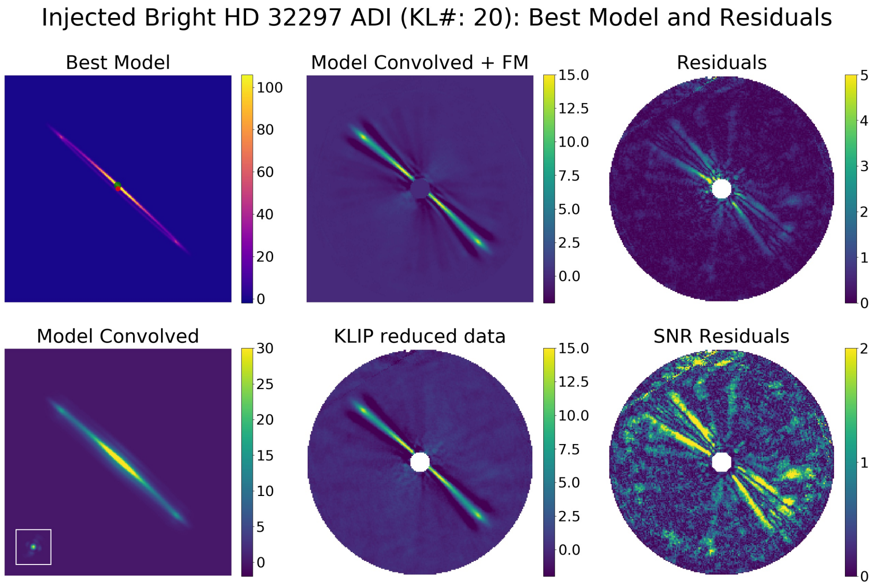

(b) Fits to mock data using 20 KL basis vectors

Figure 2.10: Results of the injection of brighter (upper) and dimmer (lower) edge-on disks. The images in the lower panel are mock datasets in which a model-generated desk was injected into a GPI dataset. The lower middle pane images are the result of the KLIP reduction of the injected frames. The upper middle and left panels shows the best fit model to the KLIP dataset using forward modeling. The right panels show the residuals between the KLIP model and simulated data.

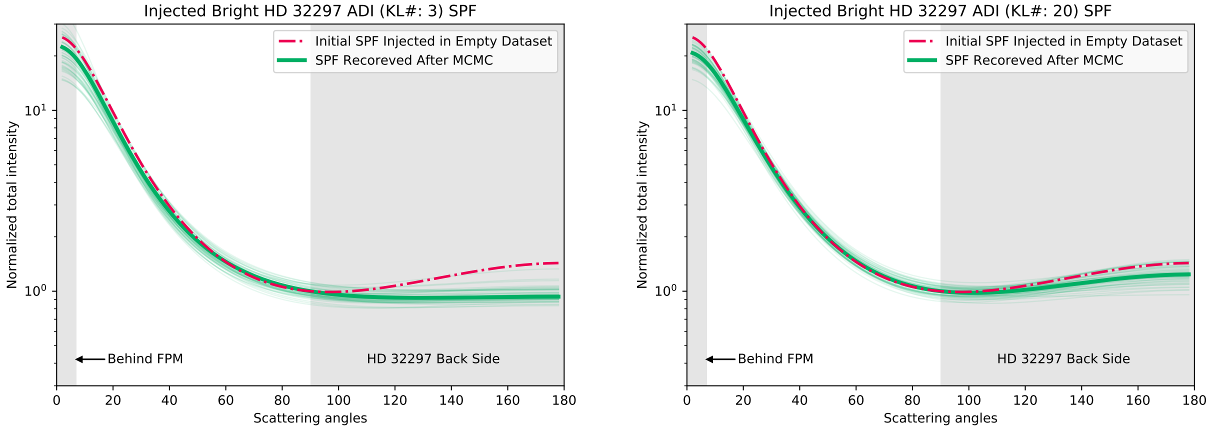

(a) SPFs fitted to an image with 3 KL basis vectors subtraction

(b) SPFs fitted to an image with 10 KL basis vectors subtraction

Figure 2.11: SPF of the input edge-on model disk shown in Figure 2.10 and SPFs of walkers of the MCMC fits.

CHAPTER 3

Multiband Polarimetric Studies of the HR4796a Debris Disk

3.1 Introduction

HR4796A is a well-studied debris disk surrounding a 9 Myr (Bell et al., 2015) A0V star, at a distance of 71.91 ± 0.70 pc from Earth (van Leeuwen, 2007; Gaia Collaboration et al., 2016). The disk is exceptionally bright with an infrared excess $f = L_{IR}/L_{*} = 5 \times 10^{-3}$ (Jura, 1991) which has made it a popular target for subsequent debris disk studies. Since its discovery the disk has been imaged in many wavelengths including the sub-mm (Sheret et al., 2004), the mm (Greaves et al., 2000), mid-infrared (Koerner et al., 1998; Lisse et al., 2017), near-infrared (Schneider et al., 1999; Perrin et al., 2014; Milli et al., 2017), and visible (Schneider et al., 2009, 2014; Milli et al., 2019). These multiwavelength observations have allowed for extensive modeling of the spectral energy distribution (SED) in order to understand the dust composition of the disk (Li & Lunine, 2003; Rodigas et al., 2015). Later studies have resolved a circular disk component at a radius of $\sim$77 au with a sharp radial profile and a $\sim$1 au offset from the star (Schneider et al., 2009). Modeling the exact geometry of these features reveals insights regarding the dynamics of the system (Wyatt et al., 1999; Wyatt, 2008; Nesvold & Kuchner, 2015).

Resolved imaging provides addition information about the system through studies of the wavelength-dependent scattering phase functions (SPFs) of the disk-scattered light. Early total intensity high-contrast infrared images by the Gemini Planet Imager (GPI) (Perrin et al., 2014) had shown hints of an asymmetric brightness distribution with forward scattering peak, which was later fully resolved by the Spectro-Polarimetric High-contrast Exoplanet

Research Instrument (SPHERE) (Milli et al., 2017). Though models have not satisfactorily fit the near-IR SPF, such studies have allowed for the elimination of certain gran models such as scattering by submicron Mie particles.

High-contrast imaging instruments have enabled the studies of the polarized intensity of the disk. Polarized images have the advantage of not requiring PSF subtraction of the randomly polarized star's light. Hinkley et al. (2009) presented the first near-infrared detection of the disk in polarized intensity, finding robust detections at the ansae. Later images high-contrast images taken by GPI (Perrin et al., 2014) fully resolved the disk in polarized intensity. The images showed a highly asymmetric polarized intensity scattering phase function (SPF), with the disk intensity strongly peaking at the smallest scattering angle and undetected at the largest scattering angles. Recently VLT/SPHERE has imaged the polarized intensity in optical light, similarly showing an asymmetric polarized SPF. The polarized SPF in conjunction with the total intensity SPF allows for tighter constraints on the properties and composition of the scattering dust grains.

In this study, we present new J- and K_1-band total and polarized intensity images. We perform modeling on these images as well as the H-band polarized intensity image presented in (Perrin et al., 2014). We aim to expand our knowledge of the polarized and total intensity phase functions in near-IR and by proxy study the properties of the scattering grains in this system. In Section 3.2 we describe the observations and the data reduction techniques. In in Section 3.3 we then construct models parameterized only by geometric parameters remaining agnostic to any underlying physical mechanisms driving the grain orbits, the results of which are discussed in Section 3.5.3.

Having extracted the scattering phase function and polarized phase function, we then fit physical Mie and distribution of hollow spheres (DHS) grain models to our scattering phase function described in Section 3.5.

3.2 Data acquisition & processing

3.2.1 HR4796A observations

We observed HR4796A with GPI on March 22, 2014. A summary of the observations are listed in Table 3.1. Thirty-five 60 s exposures were taken in J-band ($\lambda_c = 1.24\mu$) polarimetry mode with 65° of field rotation, followed by thirty-eight 60 s exposures in the K_1-band ($\lambda_c = 2.05\mu$) mode with 43.8° of field rotation under good seeing conditions. The half-wave plate was rotated between position angles 0°, 22°, 45°, 68° throughout each sequence. We additionally used H-band ($\lambda_c = 1.65\mu$) polarimetry mode data whose acquisition and reduction is described in Perrin et al. (2014).

3.2.2 Data reduction

The raw data were reduced using the GPI Data Reduction Pipeline (Perrin et al., 2014). The raw images were dark-subtracted, flexure-corrected, destriped, and corrected for bad pixels. The orthogonal polarization spots were then extracted from each raw image to form a polarization cubes, each with two frames of orthogonal polarization. The cubes were then divided by a polarized flat field. Bad pixels were identified and replaced via interpolation. The star's position was measured using the position of reference satellite spots diffracted from starlight behind the coronagraph (Wang et al., 2014).

3.2.3 Polarized and angular differential imaging

Data taken in GPI's polarimetry mode are particularly suited for both polarized and angular differential imaging, both of which suppress the starlight and improve the contrast by orders of magnitude. For polarized differential imaging (PDI), we subtracted the two frames of orthogonal polarization for each datacube, removing the majority of the starlight which has a randomly oriented polarization. Stokes cubes were then constructed from the resultant frames using a singular value decomposition method (Perrin et al., 2014) to recover Stokes parameters from the data and HWP-modulated time-variable measurement matrices. The

Target	UT Date	Filter	Obs. Mode	No. Exps.	Field Rot. (°)	Airmass	Seeing
HR4796A	2016 Mar 23	J_coron	spec	59	48.8	1.02 - 1.03	0.4 - 0.7
HR4796A	2016 Mar 18	H_coron	spec	37	52.7	1.01 - 1.02	0.5
HR4796A	2015 Apr 3	K1_coron	spec	46	78.5	1.01 - 1.02	0.3
HR4796A	2014 Apr 22	J_coron	pol	35	65	1.03	0.3
HR4796A	2014 Apr 22	K_1_coron	pol	38	43.8	1.02	0.7
HR4796A	2013 Dec 12	H_coron	pol	11	2.1	1.3	0.2

Table 3.1: Observations

mean stellar polarization was corrected for by first measuring the average polarized intensity (Stokes parameter I) inside of the focal plane mask. The total intensity image scaled by the measured intensity was then subtracted from the linearly polarized intensity image. The final image that was fit to in subsequent modeling described in Section 3.3 was a radial polarization image, a combination of the Q and U images that gives the polarization in the radial direction. For an optically thin single scattering disk, all of the signal is expected to lie in this radial polarization.

Another advantage of using this polarization data is that the sum of the linear polarization states can be combined and processed using an angular differential imaging (Marois et al., 2006, ADI) algorithm, to produce a PSF subtracted total intensity image. For each data cube, we combined the two linear polarization states to form a series of total intensity images to correspond to each polarization image. We then used a Python implementation of Karhunen-Loeve Image Projection (Soummer et al., 2012, KLIP), PyKLIP (Wang et al., 2015), to perform this angular differential imaging. We optimized the size and number of subtraction regions, as well as the number of basis vectors subtracted, to minimize PSF self-subtraction of the disk by making measurements of the signal-to-noise (S/N) at various points along the disk as a function of KLIP parameters. Our measurements indicated the optimal parameters were one basis vector and one subtraction.

3.2.4 Spectral mode observations

Our forward model as described in Section 3.2 requires a convolution of our model with a PSF. The PSF for GPI is challenging to model, due to its complex structure and variability (Wang et al., 2014). As such, rather than use a Gaussian or Airy function, we used a PSF that extracted from the four satellite spots dispersed in each image of HR4796A. Since polarimetric frames are broadband — and are therefore have overlapping satellite spots in a single frame — we extracted the PSF structure from satellite spots of observations taken in GPI's integral field spectrograph (IFS) mode. We elected to use the HR4796A satellite spots, even though the field is noisier than that of other observations of other stars because of the dependence of the PSF shape on the stellar spectrum. The stellar spectra would affect the relative weights of the extracted satellite spots at different wavelengths. We used thirty-six 60-second H-band frames taken on March 18, 2016, fifty-eight 30 s J-band frames taken on March 23, 2016, and thirty-six 60 s K_1-band frames taken on March 13, 2016.

3.2.5 Convolution PSF construction

These data were also reduced using the GPI Data Reduction Pipeline (Perrin et al., 2014). The raw images were dark-subtracted, flexure-corrected, destriped, and corrected for bad pixels. The spectra for each spaxel were then extracted to form 3D data cubes. The data cubes were then further corrected for bad pixels and distortion.

In order to estimate the PSF, we first summed the spectral mode images along the wavelength axis and the polarimetric frames on the polarized axis, both giving estimates of the total intensity across the bandpass. We took the median image of these flattened spectral mode images and the median of the polarimetric mode images. We high-pass filtered both median images with a box size of 6 spaxels, in order to remove large-scale structure from the main image of the star behind the occulting PSF. This box size was chosen to optimize the uniformity of the background structure surrounding the star. Each spectral channel was linearly combined with a weight to find the least-square difference with the polarimetric satellite spot. The need for different weighting parameters stems from the difference in throughput between spectral and polarimetric mode. To get an image of the PSF, we registered the spectral satellite spots of each wavelength, multiplied each one by the weights we had fitted for, and summed them along the wavelength axis. The PSF is highly asymmetric, with lobes at four locations around the core. Thus our model convolution, we azimuthally averaged this PSF because each image of the disk is derotated for sky rotation, making the final PSF a combination of rotated PSFs from individual exposures.

3.3 Prescriptive Modeling

3.3.1 Model description

In order to extract the geometric parameters and brightness function of the disk, we fit a geometric model to the data. By fitting a model generated purely from an arbitrary description of phase and geometric parameters, we remain agnostic to any assumptions about the physical forces on the dust grains, the orbital grain distribution, or the properties of the dust grains. In this procedure, we additionally use KLIP forward modeling (Pueyo, 2016) to account for self-subtraction of the disk brightness in total intensity.

We selected our preferred prescription for the disk by minimizing the number of parameters needed to achieve comparable χ^2 values. We found that modeling the disk as an ellipse (as opposed to an offset circle) added extra parameters that did not improve the χ^2 sufficiently to warrant the more complicated disk. We therefore modeled the ring as a series of nested circles offset from the star. We fit for Ω, the position angle of the major axis, and i, the inclination of the nested circles.

We constructed the model by mapping each pixel location (x, y) in the sky plane to a radius $r(x, y) = \sqrt{x_{\text{disk}}(x, y)^2 + y_{\text{disk}}(x, y)^2}$ in the disk plane and a $\theta(x, y) = \tan^{-1}(x/y)$ in the sky plane. The intensity of each pixel is then

$$I(x, y) = \frac{B_r(r) B_\theta(\theta)}{r_*^2}, \tag{3.1}$$

where B_r is the radial intensity, B_θ is the azimuthal intensity profile, and r_* is the distance between the disk and the star. Here, B_θ is a periodic spline interpolation with varying numbers of knots, with the intensity at every knot as a free parameter. Transforming B_θ to B_ϕ where ϕ is the scattering angle gives the SPF of each model disk.

The knots are evenly spaced in the sky plane along the disk, as shown in the blue points in Figure 3.1. By spacing the points with a separation larger than the scale of the PSF, we minimized the effects of spatially correlated noise residuals. To find the optimal number of spline points, we used the dust modeling package MCFOST (Pinte et al., 2006a) to generate a model with similar geometry to HR4796A and a known two-component Henyey-Greenstein

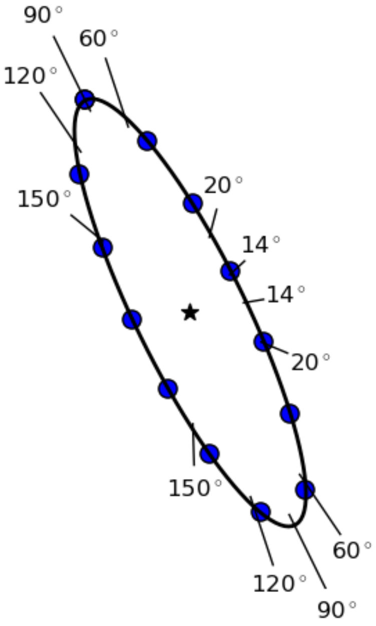

Figure 3.1: Blue points indicate the locations of the spline points of the intensity of the disk around the disk. The number of spline points was determined to be the minimum number of points to recover a known SPF to a 1% level. The marked angles are the scattering angles assuming that the west side is closer to the observer. The extracted polarized phase function was cut off at a scattering angle of 120° where the disk signal falls below the noise level. The total intensity data was truncated at angles less than 20° and greater than 150°.

phase function with the dust modeling package MCFOST. We then injected this model into a separate polarization dataset with no disk detection. We used our modeling procedure to recover this artificial disk. Transforming the recovered B_θ to B_ϕ gave a curve that could be directly compared to a theoretical B_ϕ scattering phase function. Using a minimum number of 13 knots we were able to recover the scattering phase function to the 1% level at all observable scattering angles. Though the locations of the spline points are not densely sampled in ϕ vs B_ϕ space, as long as the intrinsic SPF is smooth, the spline will recover its shape at all accessible scattering angles. This is in contrast to extractions of an SPF that use aperture photometry to sample to the brightness B_θ which can only be described by brightnesses at the discrete locations of the apertures and suffer from self-subtraction bias.

The radial profile B_r is a broken power law:

$$B_r(r) = \begin{cases} c\left(\frac{r}{r_0}\right)^{-\gamma_{\text{in}}} & \text{if } r_{\text{in}} < r < r_0 \\ c\left(\frac{1}{r_0}\right)^{-\gamma_{\text{in}}}\left(\frac{r}{r_0}\right)^{-\gamma_{\text{out}}} & \text{if } r_0 < r < r_{\text{out}} \\ 0 & \text{otherwise} \end{cases} \tag{3.2}$$

where r_0 represents the central radius in milliarcseconds, γ_{in} the inner radial profile and γ_{out} the outer radial profile, as free parameters. The radial profile was found to be very sharp, to the point that the γ factors were degenerate with the inner and outer radii. To reduce the number of parameters and avoid unbounded parameters, r_{in} and r_{out} were fixed at 70 and 100au, respectively. These radii were selected by deprojecting the disk and finding the radii where the S/N of the disk falls below 10%.

3.3.2 Fitting procedure

We then used our model disks to fit to the J- and K_1-band total and polarized intensity images, as well as H-band polarized intensity image. The H-band total intensity did not have enough field rotation to reliably be forward modeled. We created model images with the above parameters, which we then convolved with our derived convolution PSF. In order to simulate the effects on the final data product due to the KLIP PSF subtraction, we developed the DiskFM module for PyKLIP (Wang et al., 2014), specifically for forward modeling extended objects based on the mathematical framework presented in Pueyo (2016). Due to this extra step of modeling, we fixed the geometrical parameters of the total intensity disks to those found from their polarized intensity counterparts and only fit the scattering phase spline function. This is a natural choice as the total and polarized intensity images are generated from the same raw data images.

We fit each disk's geometric parameters independently from band to band, to account for various physical and nonphysical effects. The position angle of the line of nodes (Ω) and inclination (i) could differ between bands, as there is some uncertainty in the rotation of the instrument relative to north. The radial profile parameters were fitted separately to reflect possible changes between the distributions of differently sized dust grains due to differing effects of radiation pressure and gravitational forces.

We independently fit the by using a linear least-squares algorithm to optimize the χ^2 using the uncertainty maps. We then used the resultant parameters to seed a fit using an ensemble Markov chain Monte Carlo (MCMC) using the *emcee* package (Foreman-Mackey et al., 2013). The final geometric parameters are shown in Table 3.2 with their error bars derived from the distributions of the final walkers. After fitting for the geometrical parameters, we fixed all of the geometrical parameters for each model disk and fit only the spline parameters.

3.4 Disk geometry results

3.4.1 Geometric parameters

The data and best-fit models for the polarized intensity data are shown in the left and middle columns of Figure 3.3. The third column shows the difference between the final and data images divided by our noise map. The residuals for the H- and K_1- band model are consistent with the data estimated data uncertainties. Some residual structure may be seen in the J-band image northeast ansa, which we will later discuss in Section 3.4.2.

Fits to the total intensity data are shown in Figure 3.4. The northwest portion in the

Parameter	K_1 Pol	H Pol	J Pol	Milli 2017	Schneider 2018
PA	27.12 ± 0.12	27.14 ± 0.12	27.59 ± 0.12	27.1 ± 0.7	26.37 ± 0.22
i	76.53 ± 0.08	76.57 ± 0.15	76.91 ± 0.12	76.45 ± 0.7	75.92 ± 0.14
γ_{out}	-15.87 ± 0.19	-14.13 ± 0.21	-13.58 ± 0.12		
γ_{in}	42.5 ± 0.79	54.73 ± 0.66	37.0 ± 0.30		
ω	-70.37 ± 0.38	$-72.9 \pm .33$	-62.6 ± 0.18		
offset (mas)	52.01 ± 0.49	62.370 ± 12.24	17.04 ± 13.31		
r_0 (mas)	1062 ± 3.19	1053 ± 3.65	1064 ± 3.45	1064 ± 6	1059 ± 4.6

Table 3.2: Notes. We chose to fit the PA and inclination separately for each disk in order to account for uncertainty in rotation of the instrument relative to north due to the instrument being in different cycles, as well as differences due to flexure. Furthermore, we fit the radial profile parameters to account for possible differences in the structure of the disk of different grain sizes. The fifth column lists the parameters found, averaged over the H, H2, and H3 bands, by Milli et al. (2017), and the sixth lists the average parameters found by Schneider et al. (2014) with the F25ND3 filter. The radius for Milli et al. (2017) is the average distance from the star of points along an ellipse with a semimajor axis $a = 1.066$" and an ellipticity $e = 0.07$.

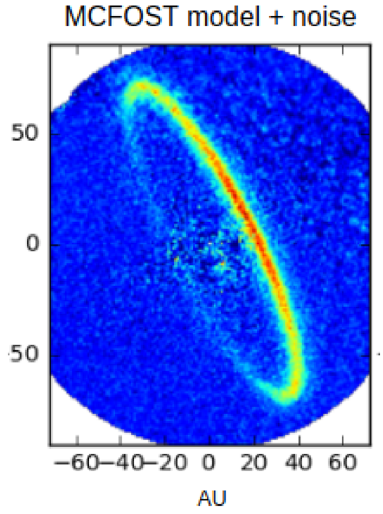
MCFOST model + noise
50
0
-50
−60−40−20 0 20 40 60
AU

(a) HR4796a-like disk generated by the MCFOST code with a known Henyey-Greenstein function injected into a noise map.

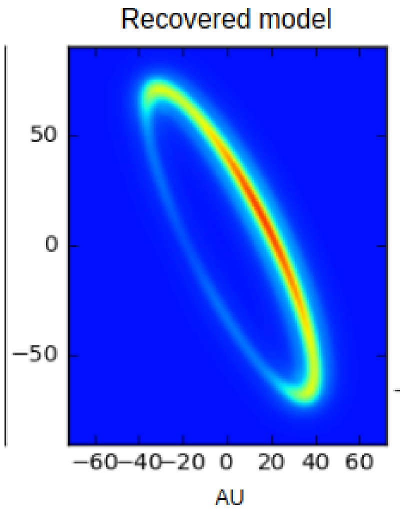
Recovered model
50
0
−50
−60−40−20 0 20 40 60
AU

(b) Recovered model using fitting code with the optimal spline parameters.

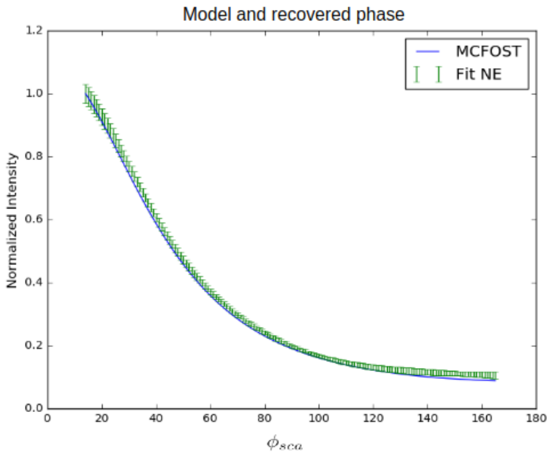

(c) Recovered model and input MCFOST model

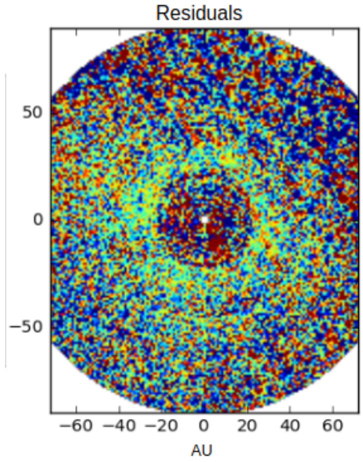
Residuals
50
0
−50
−60 −40 −20 0 20 40 60
AU

(d) Residuals of injected disk and recovered model

Figure 3.2: Injection and retrieval of a disk with a known Henyey-Greenstein model.

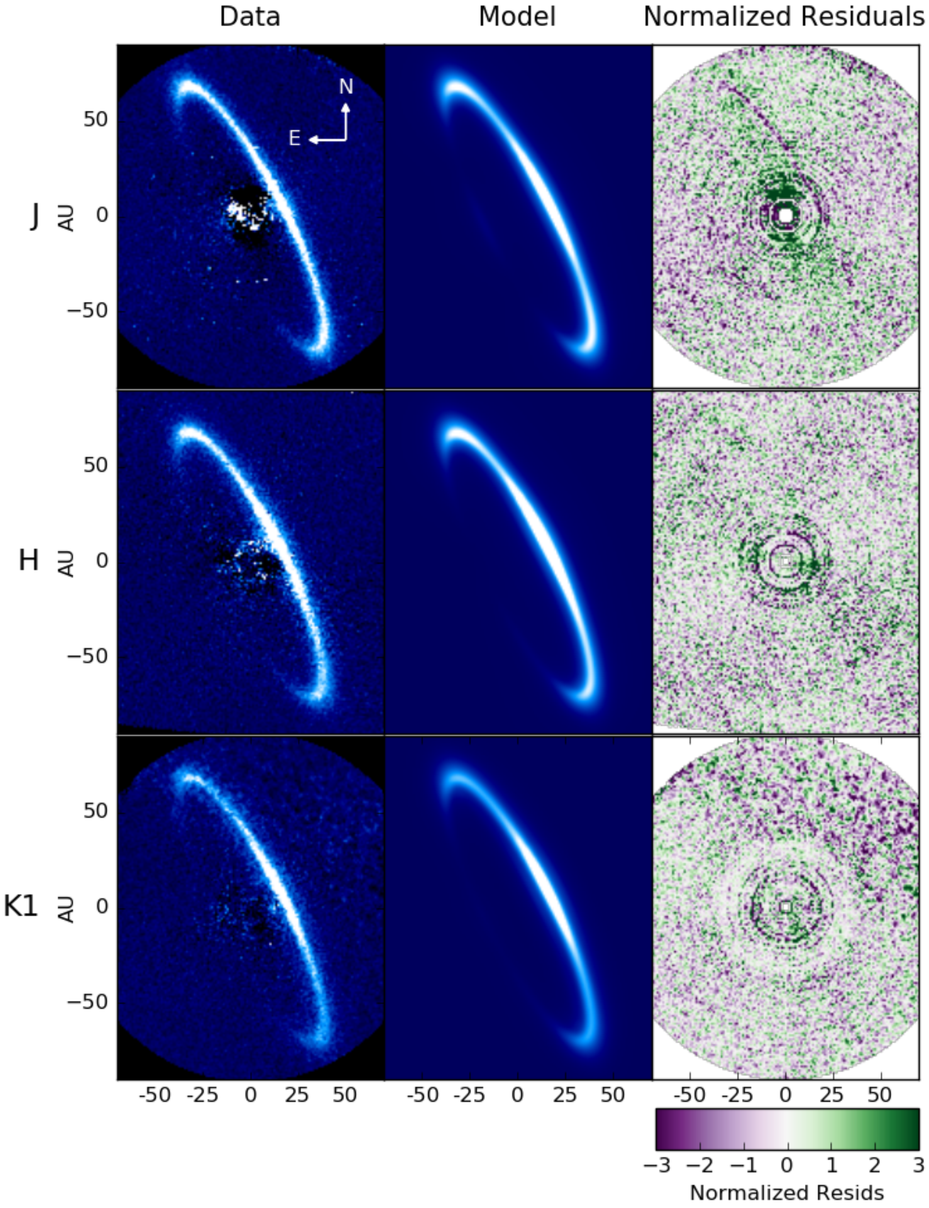

Figure 3.3: The left column shows the data, while the middle column shows the best fit model for the polarized intensity image. The right column shows the model subtracted from the data divided by the noise map. While most of the normalized residuals indicate per-pixel χ^2 under 1, the *J*-band image shows some structure.

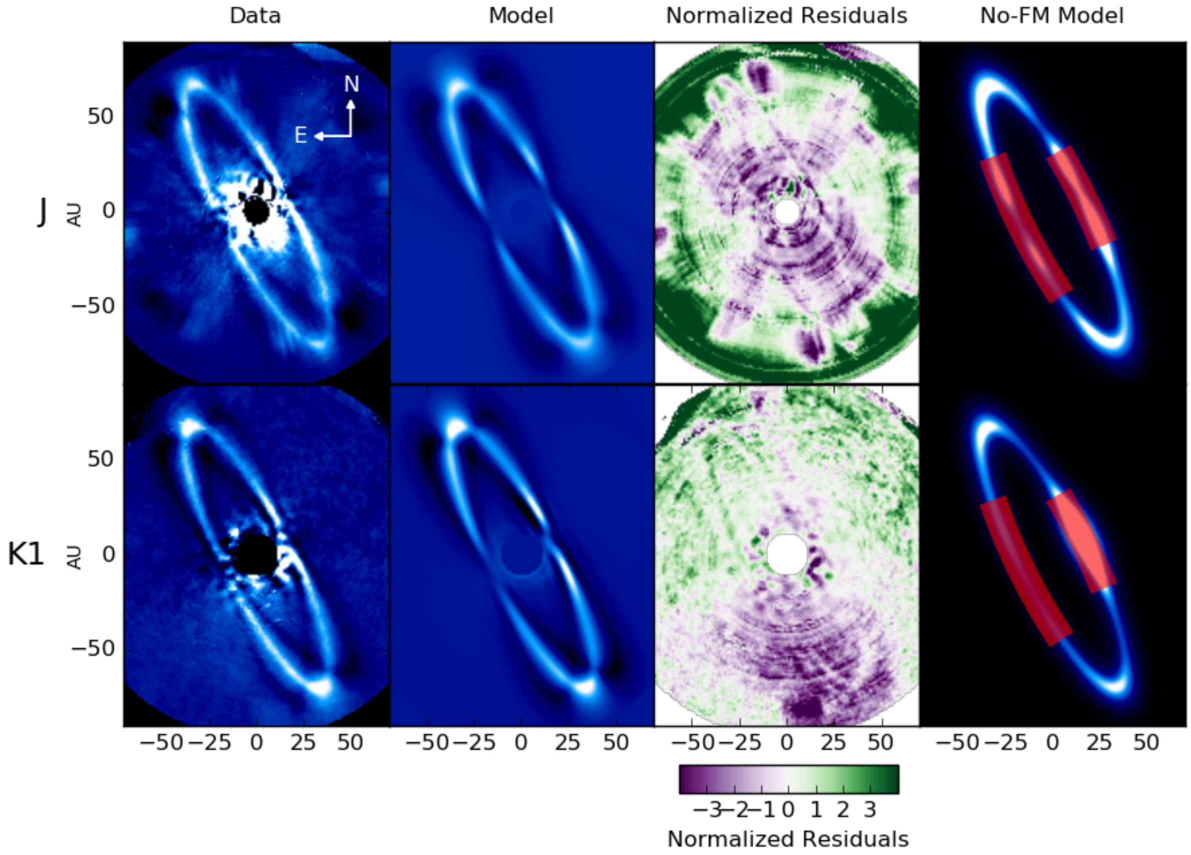

Figure 3.4: Left column: KLIP PSF-subtracted J- and K_1-band data images. Middle left column: best-fit forward model. Middle right column: forward model subtracted from data divided by the noise map. Right column: convolved model before forward modeling. The shaded regions indicate areas we have omitted in our phase curve fits. Upper row: K_1band. Lower row: Jband. We chose not to fit to the Hband total intensity due to the small amount of field rotation.

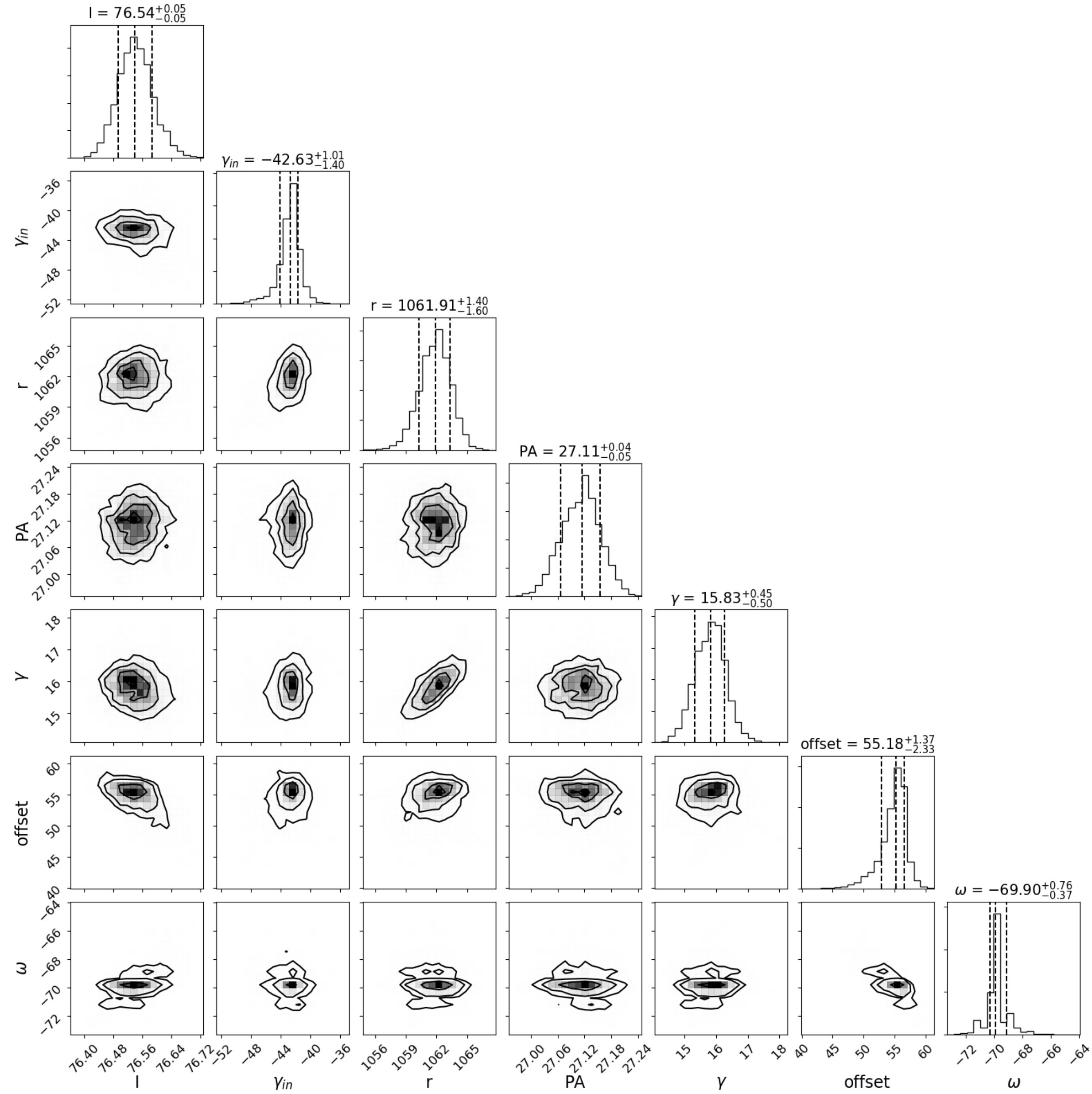

Figure 3.5: Probability density distribution for the K_1-Pol parameters shown in Table 3.2. H-band and J-band polarized intensity show similar structure, though with wider distributions due to lower signal-to-noise.

J-band image overfitted to speckle noise, most evident inn the image of the model without modeling whish shows an unphysical dip intensity. Because of this, we have decided to omit the J-band polarized fraction and total intensity curves from the phase curve analysis in Section 3.5.

The final distributions of the MCMC walkers for the K_1-band fit are shown in Figure 3.5, and the best-fit parameters with 3σ variance for all bands are listed in Table 3.2. It is evident from both of the walker distributions in Figure 3.5 that the variance of the final parameters are unrealistically small, most likely due to some model mismatch. In the final values for the PA and ω (the direction of the offset), listed in Table 3.2, we have included the variance of the image from true north of $-1^\circ \pm .001^\circ$ found by Konopacky et al. (2014). Calculations of the radius in milliarcseconds shown in the last line of the table have included the error in assumed plate scale of 14.14 ± 10^{-5} milliarcseconds.

Table 3.2 also shows comparisons to parameters found by Milli et al. (2017) in Hband and Schneider et al. (2014) in the F25ND3 filter. Milli et al. (2017) found their geometric parameters by fitting radial profiles to cuts of the image and fitting ellipses through the maximal radial values of every profile. To compare with our circular model, Table 3.2 shows the average distance of every point along the ellipse to the star with their best-fit parameters of a semi-major axis $a = 1.066$" and ellipticity $e = 0.07$. As the J-band image has strong residual structure that is likely driving the fit parameters, it is more useful to compare parameters between K_1- and H-band parameters. The geometry parameters of the position angle and inclination in these bands are consistent not only with each other but also with Milli et al. (2017). The radii found in Milli et al. (2017) are consistent with our derived K_1- and J-band models, but not with the H-band model. This may be due to biasing of fit by noise close to the focal plane mask in the Hband. Overall, the most consistent and reliable geometric measurements come from the K_1band.

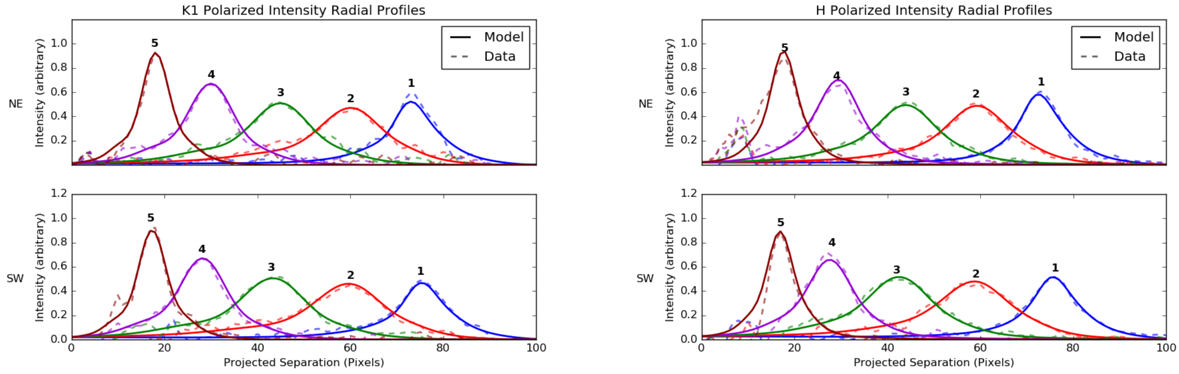

(a) K_1-band (b) H-band

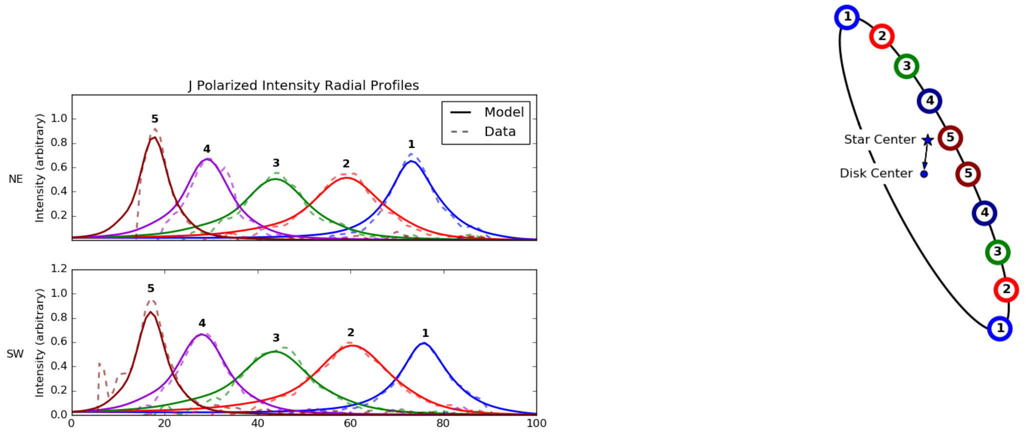

(c) J-band

(d) Projected radial locations of the radial cuts taken

Figure 3.6: Radial cuts of the data and model. Each of the data and model images were rotated such that the x-axis aligned with one of the radial locations marked in (d), which additionally shows the direction of the star center from the disk center with an exaggerated distance. A horizontal cut 4 pixels deep along the x axis were summed along the vertical axis. The solid lines show the cuts of the model images while the dashed lines are the cuts of the data images at each of the radial locations.

3.4.2 Radial profile

The inner radial profile exponents γ_{in} are large, indicating an unresolved inner edge. The error bars are unrealistically small due to nonuniformity in the radial profile, with one ansa forcing a steeper radial profile and the other forcing a broader radial profile. This effect is most visible in the J-band residual image in the northern portion of the disk in the upper left panel of Figure 3.3. There are residuals between the data and the model exactly at the midplane, and a visual inspection of the J-band data and model show that this is likely due to the data's radial profile being sharper in that region. A more direct representation of the radial profile can be seen in Figure 3.6d, in which we plotted the intensity radially along the cuts in the directions shown in Figure 3.6d(d). The K_1-band radial profiles in Figure 3.6d(a) show little systematic deviation between the model and data. In the H-band radial profiles, the radial profiles near the ansae are well-fit, though there is evidently noise at small scattering angles near the focal plane mask. This is a likely explanation for the small radius in the H-band fit. In J-band shown in Figure 3.6d(c), the southwest radial fits are good, but the peaks of the model cuts are systematically lower than those of the data in the NE region. The radial profile fit is forced by the inner and outer sides of the profiles, lowering the peak. As the model's radial profile is uniform about the disk, this indicates that the radial profile in the northeast half of the disk is sharper than in the southeast half. Such an effect would be seen most evidently in J-band as it has the smallest PSF and highest resolution. Qualitatively, the narrowing of the disk in the north-west side is consistent with the Olofsson et al. (2019) measurements of polarized SPHERE/ZIMPOL data. We refer the reader to Olofsson et al. (2019) for an in-depth discussion of the physical mechanisms that may be causing this effect.

3.5 Phase function

3.5.1 Phase curve extraction results

The polarized intensity curves are shown in Figure 3.7, normalized at a scattering angle of 90°. The scattering phase functions are strongly forward-scattering with both the polarized and total intensity phase curves peaking at the smallest scattering angles. The NE and SW curves in the $H$and K_1bands are symmetric, while the NE ansa of the J-band image has a bump at a scattering angle of 55° due to the residual structure seen in the images at this scattering angle. While the phase curves have similar behavior from $70° - 120°$, the heights of the peaks vary with wavelength. The K_1-band phase curve ($\lambda_c = 2.05\mu$) evidently has a sharper forward scattering peak than the Hband's ($\lambda_c = 1.65\mu$) which is sharper than the Jband's ($\lambda_c = 1.12\mu$). Polarized intensity phase curves taken by ZIMPOL at $\lambda_c = 0.74\mu$ shows that this effect extends to smaller wavelengths, with the phase curve similarly decreasing from $80° - 120°$ but plateauing from $13° - 80°$ (Milli et al., 2019). The source of this chromaticity is unknown, as it is plausible for the effect to be caused by a different spatial distribution of multiple grain populations or chromatic effects of a single dust population. Since we are only analyzing the polarized intensity and not the polarized fraction of the J- and H-band datasets, consistency cannot be checked for chromatic effects with modeling.

The K_1-band total intensity and polarized fraction curves are shown in the middle and bottom panels, respectively in Figure 3.8. The total intensity curves were normalized at 1 at 90°, while the polarized fraction is unitless. Though it is challenging to measure the polarized and total intensities in physical units, the unnormalized curves can be divided to calculate the polarized fraction. Consistent with phase curves in a similar band in Milli et al. (2017), the total intensity phase curve exhibits a forward-scattering peak and a flat that rises at scattering angles larger than 70°. The polarized fraction curve peaks at $\sim 40°$ at 50%, consistent with the lower limit found by Hinkley et al. (2009) of 44% as well as the peak polarization polarization of 50% at a scattering angle of 50°. found by Perrin et al. (2014).

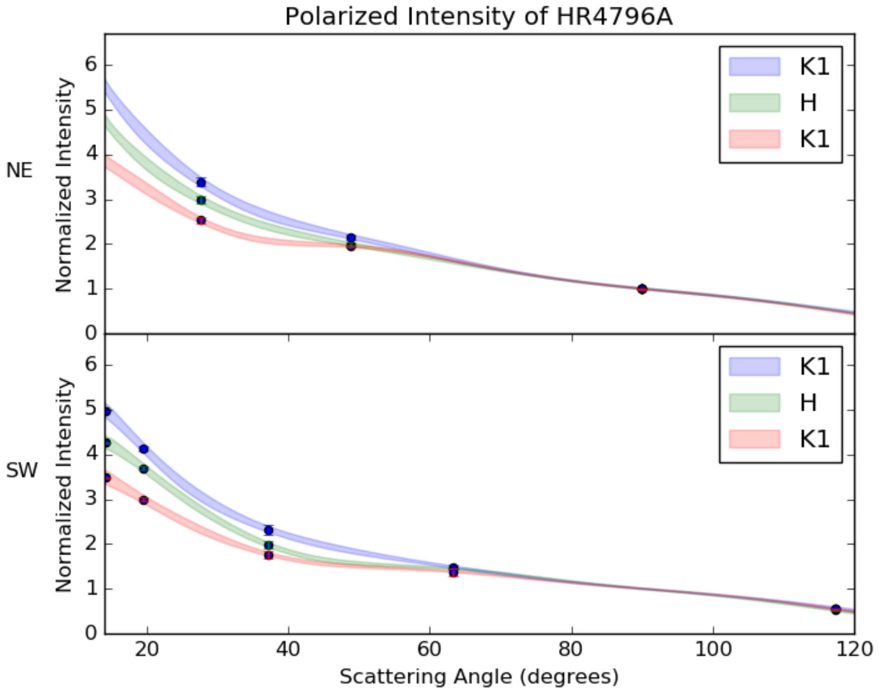

Figure 3.7: Model led polarized intensity phase curves as a function of scattering angle. The data points show the locations of the fitted spline points. The 3-σ data point error bars are overlaid, but are smaller than or equal to the size of the points. The shaded regions represent the 3-σ range of the phase curve, derived from the scatter of the splines generated from each MCMC walker's spline point values. The curves are truncated at 120° where the signal is dominated by the noise.

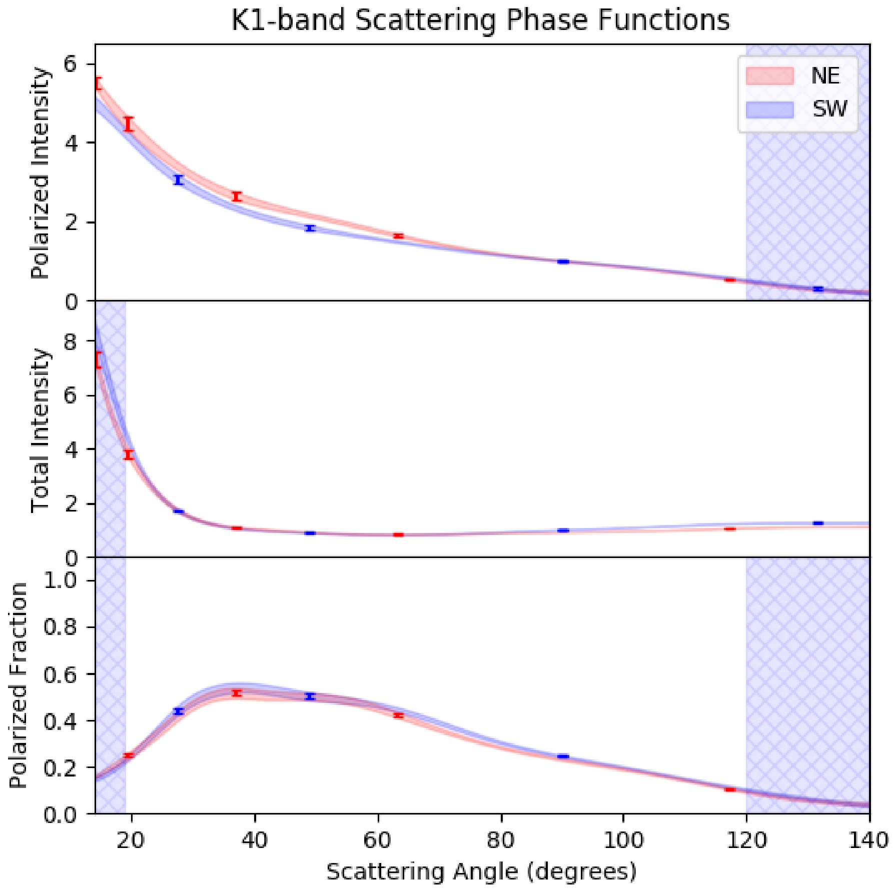

Figure 3.8: Upper panel: K_1-band polarized intensity phase curves. Lower panel: K_1-band total intensity phase curves. These curves are normalized at 13° and the error bars are derived from the scatter of the MCMC walkers' splines. The shaded portions at 20° and 140° were excluded from analysis where the signal to noise is low due to attenuation by the PSF subtraction. The data points indicate the locations of the curve spline points. Lower panel: K_1-band polarized fraction. The polarized fraction is derived by dividing the unnormalized polarized intensity phase curve from the unnormalized total intensity phase curve. The south-west curves are plotted in blue, while the north-east curves are plotted in red.

3.5.2 Dust grain modeling

We used the MCFOST package (Pinte et al., 2006b) to generate theoretical Mie and DHS phase functions (Min et al., 2005) to fit to our measured phase functions. We modeled to our highest-fidelity curves: the southwest K_1-band total intensity and the polarized fraction. We used MCFOST to compute total intensity and polarized fraction phase curves using a given set of parameters at the central wavelength of the K_1-band filter. Because the change in grain properties over the K_1-band filter is small for most materials, integrating over the whole band did not significantly affect the morphology of the curve. For the total intensity curves, we compared the data to a scaled model where we found the scaling factor by taking the ratio of the model and data curves at every scattering angle and taking the median of those ratios.

Using the scaled total intensity curve and the polarized fraction, we then computed reduced χ^2_ν values for each curve. As the profiles were generated from a previous fitting procedure, we expected the errors to be correlated, but that was ignored in this χ^2 calculation. In the total intensity fit, we excluded regions at scattering angles smaller than 20° and larger than 140°, as the data are unreliable close to the focal plane mask (shown in Figure 3.8). We truncated the polarized fraction curve past 120°, as the signal of the polarized intensity is undetected. The locations of these cut-off scattering angles with respect to the disk are shown in Figure 3.1.

We ran a grid search over the minimum grain sizes a_{min}, the exponent of the power law that describes the grain size distribution a_{exp} and the grain composition. We assumed a grain size distribution of:

$$\frac{dN}{da} \sim \begin{cases} a^{-a_{\mathrm{exp}}} & \text{if } a_{\mathrm{min}} < a < a_{\mathrm{max}}. \\ 0, & \text{otherwise.} \end{cases} \tag{3.3}$$

We parameterized the grain composition in terms of the real and imaginary component indices of refraction of the dust grains. By doing so, we remain agnostic to the chemical composition of the grains. We also eliminate the need for the porosity parameter, whose effects are captured by the real and imaginary indices of the dust grain population, assuming

Parameter	Start	End	Number of Points	Spacing
Minimum Grain Size (μm)	.01	100	15	log
Grain Size Exponent	2.5	6	10	linear
Real Index of Refraction	1.1	4.05	20	linear
Imaginary Index of Refraction	10^{-5}	10.	15	log
Scattering law	DHS/Mie			

Table 3.3: Note: The real and imaginary indices of refraction were chosen to reflect limits seen in physical grain models at the central wavelength of $2.15 \mu m$

a uniform effective medium.

The ranges of our fitting parameters are shown in Table 3.3. The phase curves were integrated over a range from $a_{\rm min}$ to $a_{\rm max}$. The maximum grain size, $a_{\rm max}$ was fixed at 1 mm due to the sharp power law that dictates that there are few large grains for any of the proposed grain size distribution. The limits of the real and imaginary indices of refraction were gained from the ranges of the indices for physical grain compositions at the K_1-band wavelength. Measured real and imaginary indices for a variety of different materials at K_1band are shown in Figure 3.12. Whereas the usually assumed exponent $a_{\rm exp}$ for the grain size power law distribution is usually assumed to be 3.5, following Mathis et al. (1977), we fit over 10 different power laws.

3.5.3 Dust grain modeling results

We evaluated both DHS and Mie models for the grid defined in Table 3.3. We examined the results of the resultant curves for each model, using the metrics of the lowest χ_ν for the total intensity curve, lowest χ_ν for the polarized intensity curve, and lowest χ_ν for both curves simultaneously. The ideal model needs the three distinctive properties of the HR4796A model: a strong forward-scattering peak in the total intensity curve, a gradual increase in the total intensity curve at the backscattering side, and a peak in polarized intensity at 40°.

We found that neither model could simultaneously reproduce all of the features of both the SPF and polarized phase function. Figure 3.9 shows the best-fit models for the simultaneous χ_ν. Though not a close model in total intensity, the DHS model is able to reproduce the features of the forward-scattering peak as well as the shape of the curve in the backscattered direction. On the other hand, the DHS model is unable to reproduce the peak in polarized fraction at 40°.

While the Mie model generates a polarized fraction curve with a peak closer to that of the data, the Mie model fails to recover the magnitude of the peak in total intensity as well as the increase in intensity at backscattering angles, exhibiting instead a flat distribution at scattering angles greater than 40°.

We computed the goodness-of-fit metrics for the total intensity and polarized fraction phase curves independently of each other by calculating the χ_ν^2 of each ignoring the other. The models with the lowest χ_ν of the total intensity phase curves are shown in Figure 3.10 with the parameters listed in Table 3.4. In this case, the best-fit Mie model is able to reproduce the back scattering increase, but cannot produce a forward scattering peak sharp enough to match the model. The DHS model has a good fit to the overall curve, with a χ_ν^2 under 1. We compare the DHS χ_ν^2 of the total intensity-only fit versus the χ_ν^2 of the combined polarized fraction and total intensity fits (shown in rows 5 and 4, respectively). This comparison reveals that the total intensity fit has an improvement on the total intensity χ^2, but a drastically worse polarized fraction.

The curves produced by fitting only to the polarized fraction are shown in Figure 3.11. Both curves have overall structures similar to the data phase curves, with a peak at 40°, but they exhibit unexpectedly an unexpectedly jagged curves. Images produced by MCFOST with these phase curves do not visibly show any of this roughness, given the pixel sampling and PSF convolution. Our model, constructed assuming a smooth phase curve, would therefore be unable to detect any extra structure on the curve without overfitting.

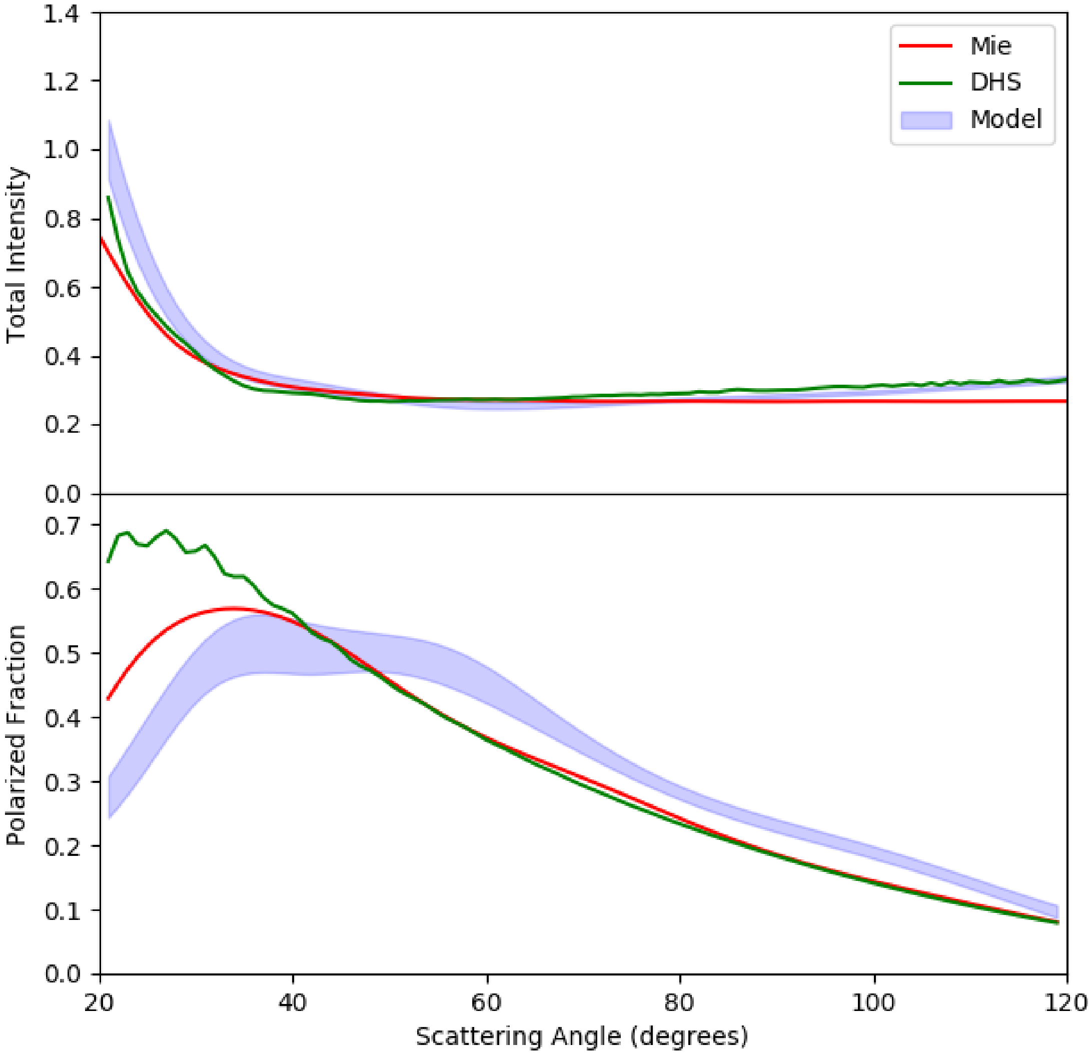

Figure 3.9: MCFOST fits of the K_1-band total intensity (upper) and polarized fraction (lower). The data-extracted curves and associated errors are shown in blue, while the red shows the best-fit curve for DHS and the green shows the best-fit curve for Mie.

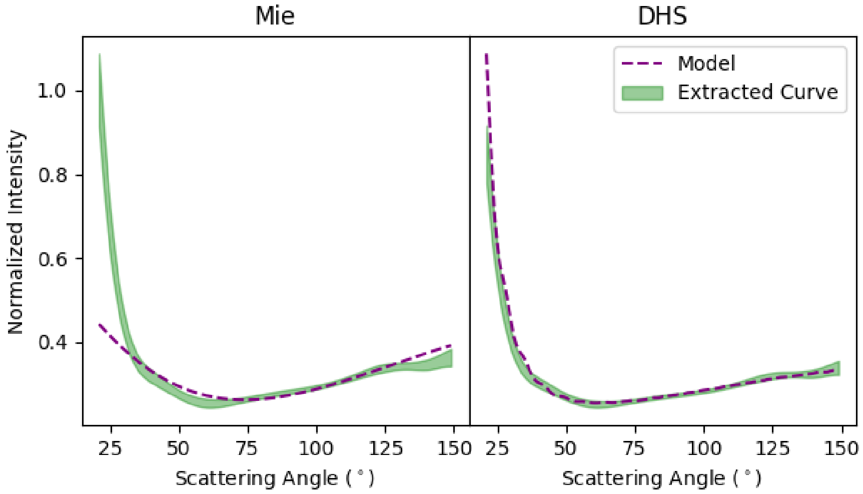

Figure 3.10: Best fit total intensity phase curves fitting only to K_1-band total intensity data for Mie theory (left) and DHS (right).

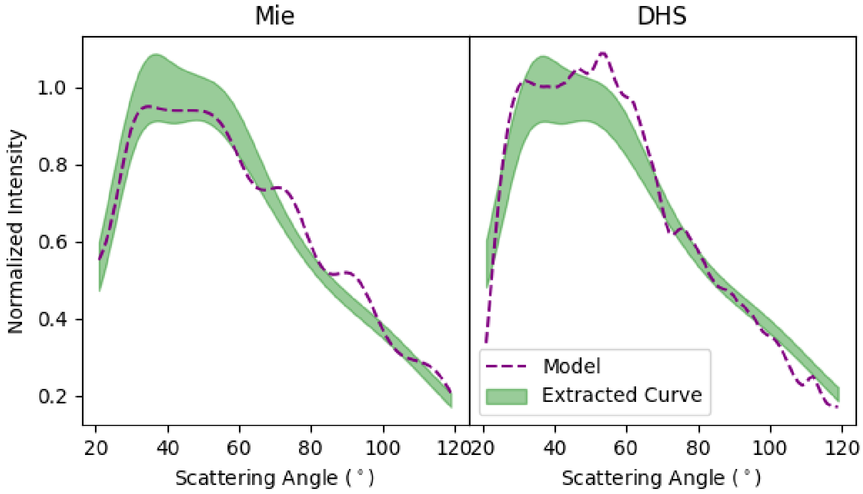

Figure 3.11: Best fit polarized fraction phase curves to only the K_1-band polarized fraction for Mie (left) and DHS (right).

Model	Metric χ^2_ν	Sum χ^2_ν	Tot χ^2_ν	Frac χ^2_ν	$a_{\rm min}$	$a_{\rm exp}$	n	k
Mie	Sum	**12.4**	13.3	11.8	1.9	2.9	3.7	3.72
Mie	Tot	155.8	**3.3**	363.1	0.3	5.7	1.1	10.0
Mie	Frac	165.2	293.6	**3.0**	3.7	3.7	2.0	2.7×10^{-2}
DHS	Sum	**11.5**	5.2	20.4	13.9	3.3	3.4	3.7
DHS	Tot	41.2	**0.8**	96.2	26.8	4.1	1.1	1.4
DHS	Frac	815.3	1458.8	**3.0**	1.9	2.9	3.4	3.0×10^{-2}

Table 3.4: Best fit parameters for different χ^2_ν for different grain models. The bolded column indicates the χ^2_ν each set of parameters was optimized for. The third column shows the sum of the total intensity and polarized fraction χ^2_νs. The fourth column and fifth columns are the χ^2_ν values for the total and polarized fraction, respectively. The second column describes the metric over which the best fit parameters were derived. The second and fifth rows list the best fit parameters in the sixth to ninth columns for the best summed χ^2_ν. The third and sixth columns are the parameters for the best total intensity χ^2_ν and the fourth and sixth list the best fit parameters for the best polarized intensity.

3.5.4 Grain indices of refraction

In order to further evaluate the generated DHS model in comparison to more physical models, we compared the phase space of likely indices of refraction we derived from our fits to indices of various other materials in Figure 3.12. Following Bruggeman mixing rules, mixtures of two or more materials result in indices intermediate to the indices of the materials being mixed. A mixture of any dust compositions would lie somewhere along the semilinear track traced out by the materials already shown. Porosity, essentially a mixture of void with a dust grain composition, would additionally move any point along the same track.

The polarized fraction DHS best fits, boxed in red, occupies a part of parameter space that is not only far from any pure dust grain composition, but would also be far from any mixture with any porosity. The parameter space of decent total intensity fits using DHS is fairly broad and overlaps with the track of physical compositions. However, the lack of overlap between the polarized fraction fits and the total intensity fits precludes any confident conclusions about the grain composition derived from the DHS fits.

3.5.5 Discussion

Both the Mie and DHS models are meant to be substitutes for more realistic — but more computationally expensive — models of aggregate dust grains. These aggregate dust grain models get exponentially more expensive with grain size. Our models that produce the smallest χ^2_ν values all exhibit large grain sizes of 2 - 26 μm, for which aggregate models have not been extensively generated. This analysis questions the validity of Mie and DHS models in producing meaningful results in this limit. The phase curves for HR4796A are unlike other phase curves in the defining features of the sharp total intensity forward scattering peak at 25 °, the modest backscattering peak and the polarized intensity peak at 25 °. Neither model was able to fully produce all three features simultaneously.

There are a number of other ways that the dust population model can be improved in future work regarding the parameterization of the size distribution. Most obviously unphysical is the sharp cutoffs of our dust grain size distribution at the minimum and maximum

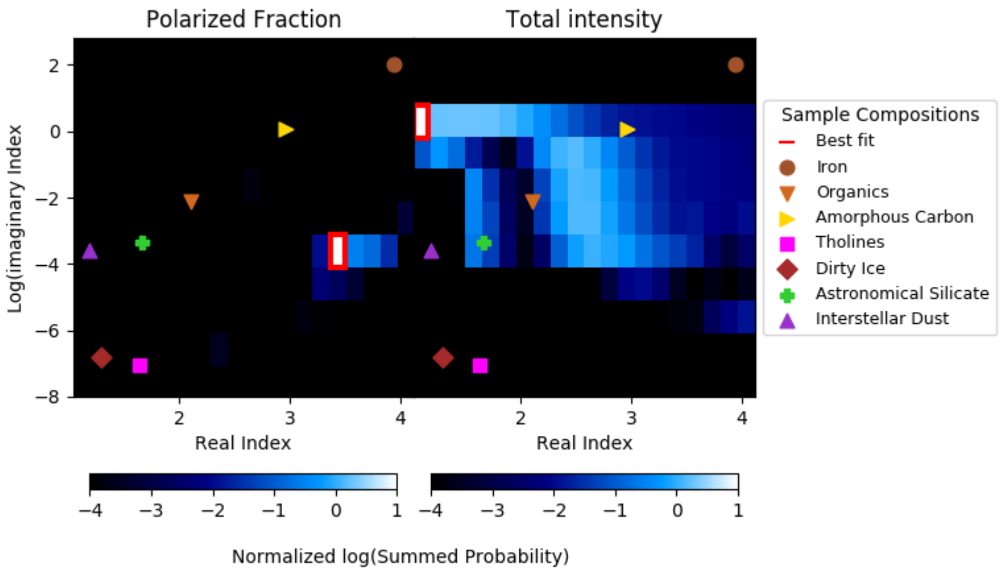

Figure 3.12: Marginalized probability maps of the DHS (upper) and (Mie) models for total intensity (left) and polarized fraction(right), gained by summing along the probability matrix along the $a_{\min}$ and $a_{\exp}$ axes. Overplotted are indices of refraction of representative dust grains (Khare et al., 1984; Pollack et al., 1994; Zubko et al., 1996; Li & Greenberg, 1997, 1998; Li & Draine, 2001)

grain sizes. Given the steep outer power law $a_{\exp}$ and our large maximum grain size it is unlikely that increasing the maximum grain size cutoff would appreciably affect the resultant model. On the other hand, creating a more gradual distribution of grains rather than one that sharply cuts off at the minimum grain size would likely affect the model phase curves. It is likely that the jagged polarized fraction phase curves would be smoothed by the inclusion of smaller grains, but not without affecting the goodness of fit to the DHS total intensity model. Another major possibility is that there is not only a mixture of grains with different compositions, but also multiple dust grain populations with different size distributions.

3.6 Conclusions

We have presented high-contrast polarimetry images of HR4796A in K_1- and J-band. Using a forward modeled disk to the polarized and total intensity, we have confirmed and put tighter constraints on the geometric properties of the disk.

The unique features of the HR4796A disk and the high S/N of our data provides some of the tightest constraints on the properties of a dust grain population, where analyses of other disks result in degenerate solutions. With our general parameterization of the dust grain properties, we are able to fully explore the phase space of grain compositions and porosities. The failure of the grid to produce simultaneous fits to the polarized and total intensity using DHS and Mie theory indicates that a more sophisicated is needed with more realistic features, such as a more physical dust grain geometry, or a more complicated dust grain population.

For future studies, we also defer analysis of the chromaticity of the polarized phase function, which evidently extends from the visible to our measurements in the near-infrared. This analysis would necessitate a better extraction of the total intensity phase function of the Jband and the Hband.

CHAPTER 4

Instrumentation

4.1 Introduction

OSIRIS (OH- Suppressing Infra-Red Imaging Spectrograph) is an instrument with an integral field spectrograph (IFS) mode as well as an imager mode designed to work with the Keck adaptive optics system Larkin et al. (2006). The imager mode has had an update of its electronics, optics and detector.

The main science goal of the upgrade was to study various aspects of the Galactic Center. Specifically, the imager is designed to provide imaging of a $19'' \times 19''$ field which will encompass seven masers in the vicinity of the Galactic Center which serve as astrometric references. High precision astrometry of this region will allow for a measurement of the precession of stellar orbits around the Sgr A* caused by general relativity. In order to detect the orbital precession of the star SO-2, we must precisely determine the location Sgr A* relative to the reference frame established by nearby masers. This precision can only be achieved by having all seven masers in the field of view. The imager additionally provides PSF references for the IFS enabling the study of sources in fields with multiple sources.

There were a number of upgrades done to improve the general image quality of the instrument. The new optics not only achieve the required field of view but also reduce the distortion allowing for more confidence in the astrometric precision. Whereas the previous imager had an oversized cold stop, the newly installed imager has a well-formed pupil with new pupil masks, discussed in Section 4.2, which are expected to increase the overall sensitivity of the instrument. Finally, we are not reusing the Hawaii 1 detector from the original OSIRIS imager, but rather a new Hawaii-2RG detector, the characterization of which is

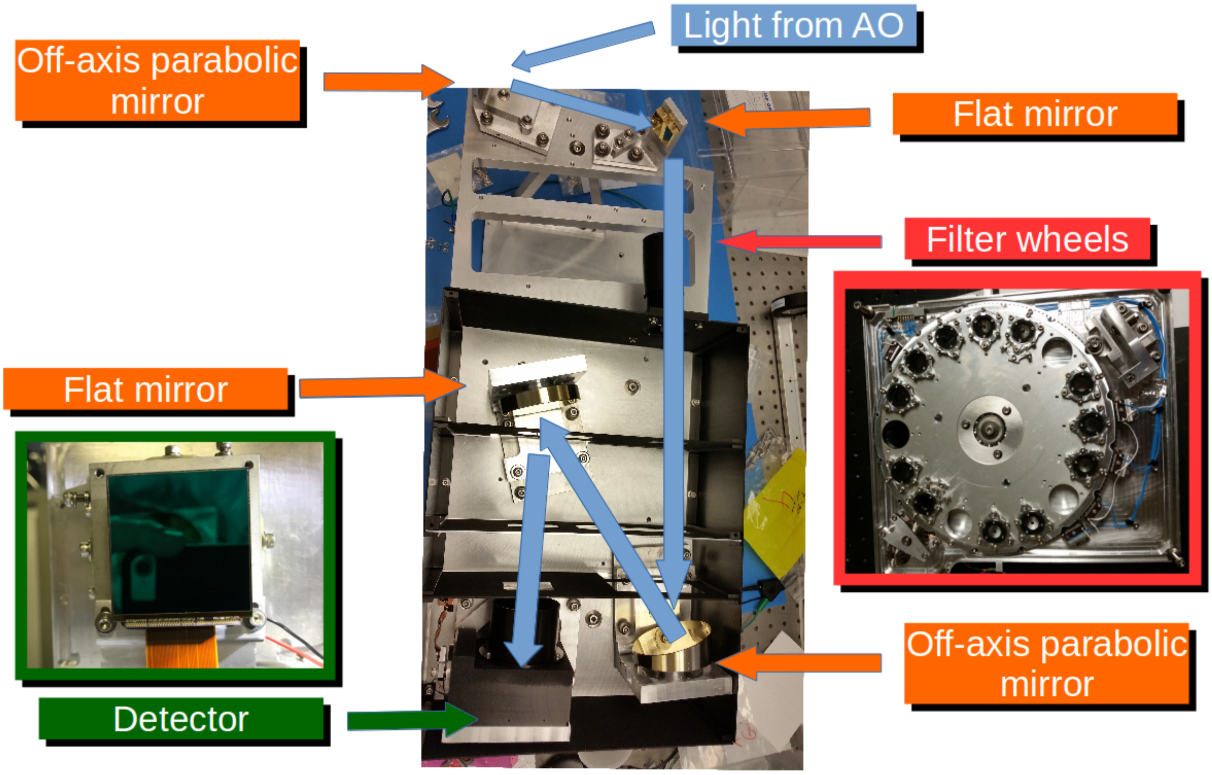
Light from AO
Off-axis parabolic mirror
Flat mirror
Filter wheels
Flat mirror
Off-axis parabolic mirror
Detector

Figure 4.1: Top-down picture of the new OSIRIS imager. The light path is indicated by the blue arrows. The relay of the off-axis parabolic mirrors (indicated in orange) achieves a field of view of $19'' \times 19''$. The design also allows for a well-formed pupil, allowing for matched pupil masks to be installed in the filter wheels (pictured in red). Finally, the new Hawaii-2RG detector is indicated in green.

described in Section 4.3.

4.2 Pupil stops

The function of a pupil stop is to block unwanted scattered light and thermal instrumental background while allowing as much of the signal's light through. In a perfect system, the shape of the optimal pupil mask would be matched to the shape of the primary mirror, secondary obscuration, and secondary support structures. However, given physical manufacturing limits, pupil nutation and rotation, and alignment errors, it is sometimes not favorable to use such a well-matched geometry. In this work, we used images from the pupil imaging mode of NIRC2 to motivate the design choices for future pupil mask construction on Keck II. We have constructed a model of the various components and their respective fluxes. We have then used those images to test hexagonal masks, to be used in the pupil tracking ”vertical angle” mode, and annular masks to be used in the sky tracking ”position angle” mode.

4.2.1 Data

Images of the Keck II pupil were obtained using NIRC2's pupil viewing mode in which a pupil imaging lens is inserted to the beam via the instrument's slide mechanism. The images were taken with the Kp, PAH and Br-α filters with integration times of 60, 1, and .18 seconds, respectively. The pupil mode only obtains a partial image of the pupil. The grism slide was translated between groups of exposures for a larger effective field of view. We took three images at each patch in each band at twilight for a total of 18 images. The sky was observed in position angle mode so the images have a slight rotation between the images. Each of the images were flat field corrected, though still exhibit some vignetting inherent to the pupil viewing mode. We did not correct for bad pixels, electing instead to exclude them from subsequent analysis. A mosaic of all 6 images in Kp band is shown in Figure 4.2. The images have a limited width and have a maximum outer radius. Regions outside of this maximum outer radius were excluded.

4.2.2 Model

The various components in the plane of the primary mirror are shown in Figure 4.3 while the components in the plane of the secondary mirror are shown in Figure 4.3. The sizes of the components were either assigned from known values or measured from the data (Le Mignant et al. 1996, Nelson et al 1985). The measured sizes are shown in Table 4.1. We constructed the model images by summing the fluxes of each of the emitting components. Additionally, we added a uniform thermal background component. We then fit our model image to the

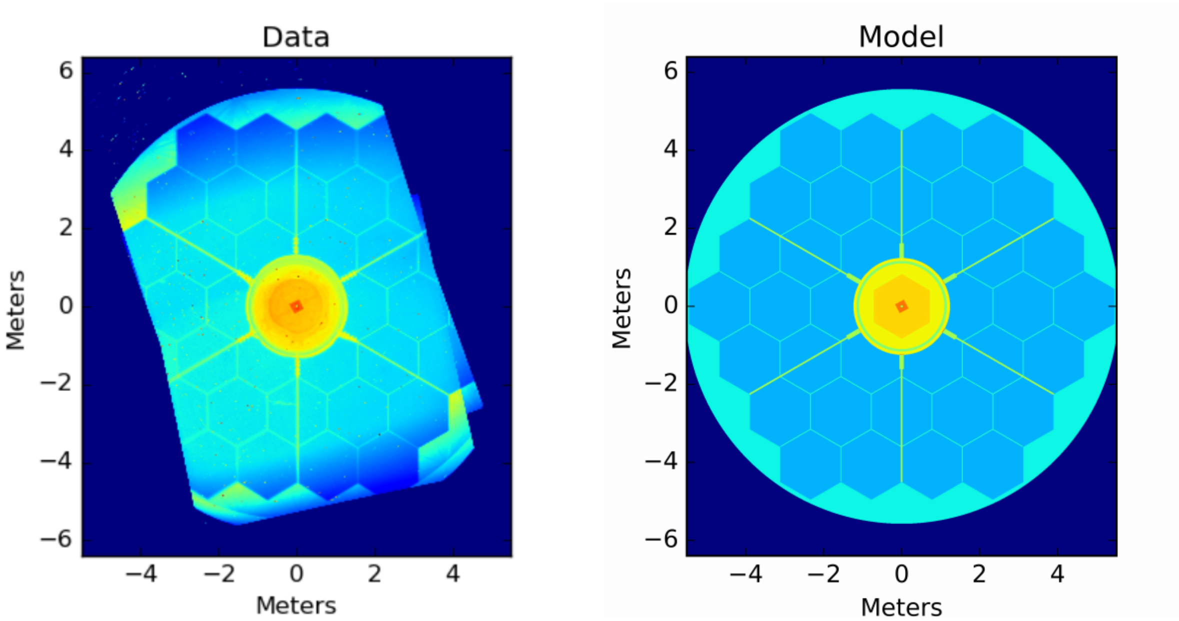

Figure 4.2: Mosiaic of the six images images taken in Kp band (left) and model fit (right)

six images in each band simultaneously by generating our model at the sampling, rotation and orientations of each data image. We masked out portions of the image which were most affected by vignetting and Gaussian blurred the images to compensate for the slight field distortion at the edges of the image. We then fit for each of the model component fluxes at each wavelength using a linear least squares algorithm.

4.2.3 Model fit

The resultant image fit in the Kp band is shown in Figure 4.2, and is well matched to the data image. The fits in other bands are similarly well fit. There were a number of degeneracies in the flux parameters which prevented us from obtaining physical fluxes of the various components. Firstly, all extended components such as the dome, secondary obscuration and sky were completely degenerate with the uniform background that arises from emission occuring far from the pupil plane — increasing the uniform background parameter decreased the flux parameters of all of the extended components. Secondly, the sky flux parameter was highly degenerate with the flux parameter of the primary mirror. The portion of the primary mirror which is not illuminated by the sky due to the secondary obscuration, shown in yellow

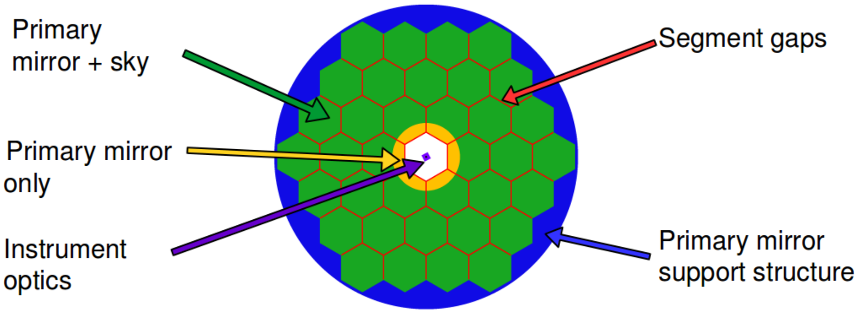
Primary mirror + sky
Segment gaps
Primary mirror only
Instrument optics
Primary mirror support structure

(a) Model components in the secondary plane. In blue, there is some thermal back-ground from the dome and support structure of the primary mirror. The green component is a combination of the primary mirror's thermal emission and the reflected sky emission. In the yellow portion, sky flux is blocked by the secondary obscura tion, so is comprised only of the primary mirror's emission. The purple box is some component in the instrument optics reflected back by the secondary mirror

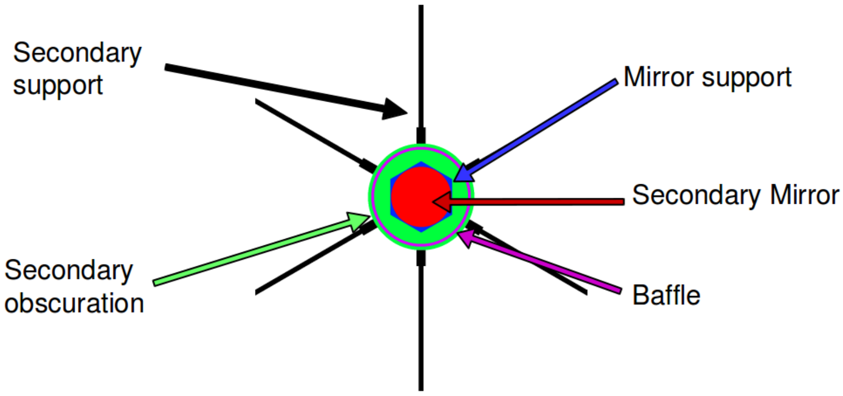
Secondary support
Mirror support
Secondary Mirror
Secondary obscuration
Baffle

(b) Components in the plane of the secondary mirror. The secondary support holds the secondary mirror scaffold shown in light green. In front of this scaffold are the baffle tube in purple, other secondary mirror scaffolding and the secondary mirror itself which are completely opaque to the emission of the secondary obscuration.

Figure 4.3: Components in the plane of the secondary mirror. The secondary support holds the secondary mirror scaffold shown in light green. In front of this scaffold are the baffle tube in purple, other secondary mirror scaffolding and the secondary mirror itself which are completely opaque to the emission of the secondary obscuration.

Component	Size (m)
Primary mirror support radius	5.56
Primary mirror segment side lengths	0.9
Instrument Optics	.035
Secondary obscuration radius	1.24
Secondary mirror radius	0.7
Secondary mirror node length	.37
Secondary mirror node thickness	.11
Secondary mirror support thickness	.035
Secondary mirror support length	.035
Baffle radius	1.12
Baffle thickness	.057
Instrument Optics	.26

Table 4.1: Dimensions of components in meters.

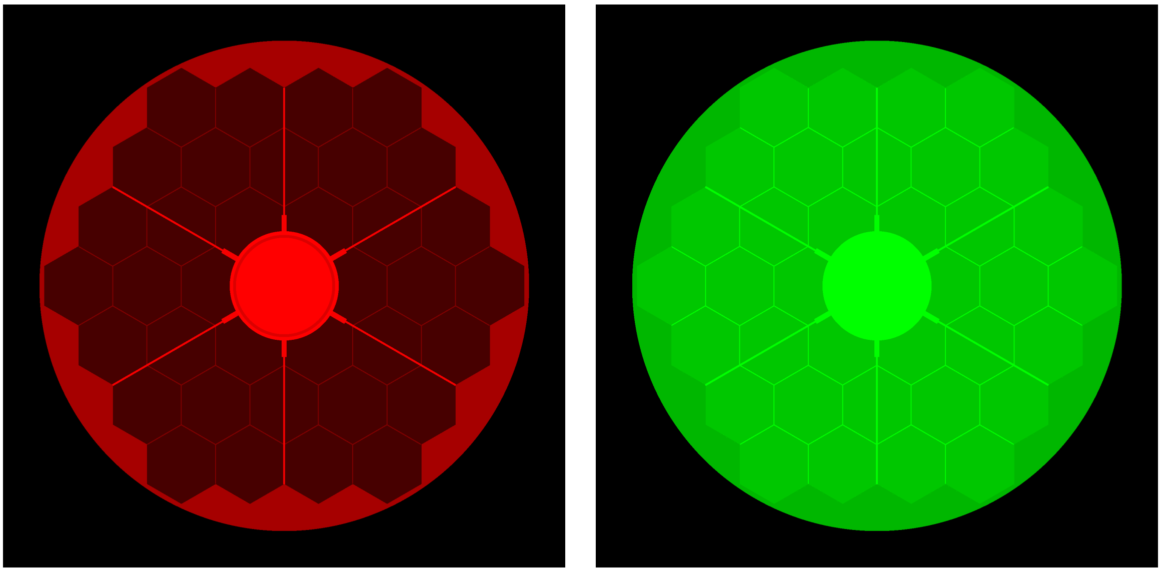

(a) Image fit for Br-α

(b) Image fit for Kp

Figure 4.4: Image fits of Br-α (4.1μm) and Kp (2.1μm). The uniform background is much more prominent in Kp, while the thermal emission is more dominant in Br-α

in Figure 2a, is very small and overlaps with many of the components in the secondary plane. Qualitative measurements of the mirror flux show it to be less than 20 ADU/pixel — on order of the image noise. Though we cannot currently convert our flux parameters into physical units, we can generally characterize the emission. In Figure 4.4, we show the fits for the longest wavelength filter, Br-α, and shortest wavelengths filter, Kp. Overall, the flux values of Br-α in units of electrons/s/μm/pixel are much larger as the thermal components emit brighter at longer wavelengths.

4.2.4 Pupil mask modeling

We modeled the background-limited signal to noise ratio using hexagonal, pupil-matched, and annular-shaped masks of varying sizes. We separately tested inner masks, which block all emission within the annulus or hexagon and outer masks, which block all emission exterior of the hexagon or annulus. The outer hexagonal mask was oriented to align with the serrated primary mirror edge while the inner hexagonal mask was oriented such that each corner aligned with a secondary support, as shown in Figure 4.6. We modeled a signal with our model of the primary mirror without the secondary obscuration, arbitrarily normalized. For each pupil mask, we nulled out anything inside or outside of the mask in the signal and noise image and summed the remaining flux. In Figure 4.5, we show the relative signal to noise of masks in Kb band for a centered mask (2.1 μm) and Br-α band (4.1 μm).

We then calculated the parameters with maximal signal to noise at 1000 shifts between the mask in the pupil plane, simulating the 1% nutation of the telescope.

4.3 Hawaii2-RG detectors

Characterization of the detector performance is critical for understanding of the capabilities of the final instrument. In this work, used data taken of a flat lamp source with a variable brightness external to the installed instrument for charaterization. We report on the gain of the detector in §4.3.1, the read noise in §4.3.2, dark current in §4.3.3, and linearity in §4.3.4.

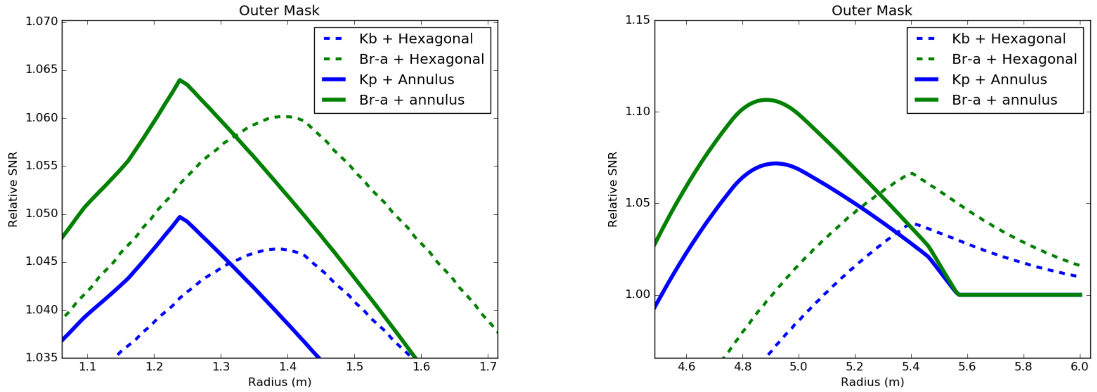

(a) Inner Mask signal to noise

(b) Outer Mask signal to noise

Figure 4.5: The relative signal to noise for Kp band (thicker blue lines) and Br-α (thinner green lines) with hexagonal masks (dashed lines) and annular masks (solid lines). The radii shown are in units of meters in the primary plane.

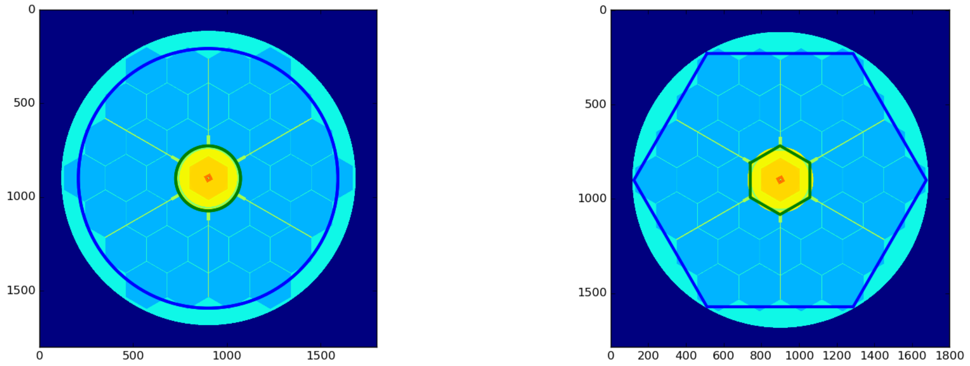
0
500
1000
1500
0
500
1000
1500
0
500
1000
1500
0
200
400
600
800
1000
1200
1400
1600
1800

(a) Example best fit circular mask.

(b) Example best fit hexagonoal mask.

Figure 4.6: The best fit inner masks for Kp in green and outer masks in blue.

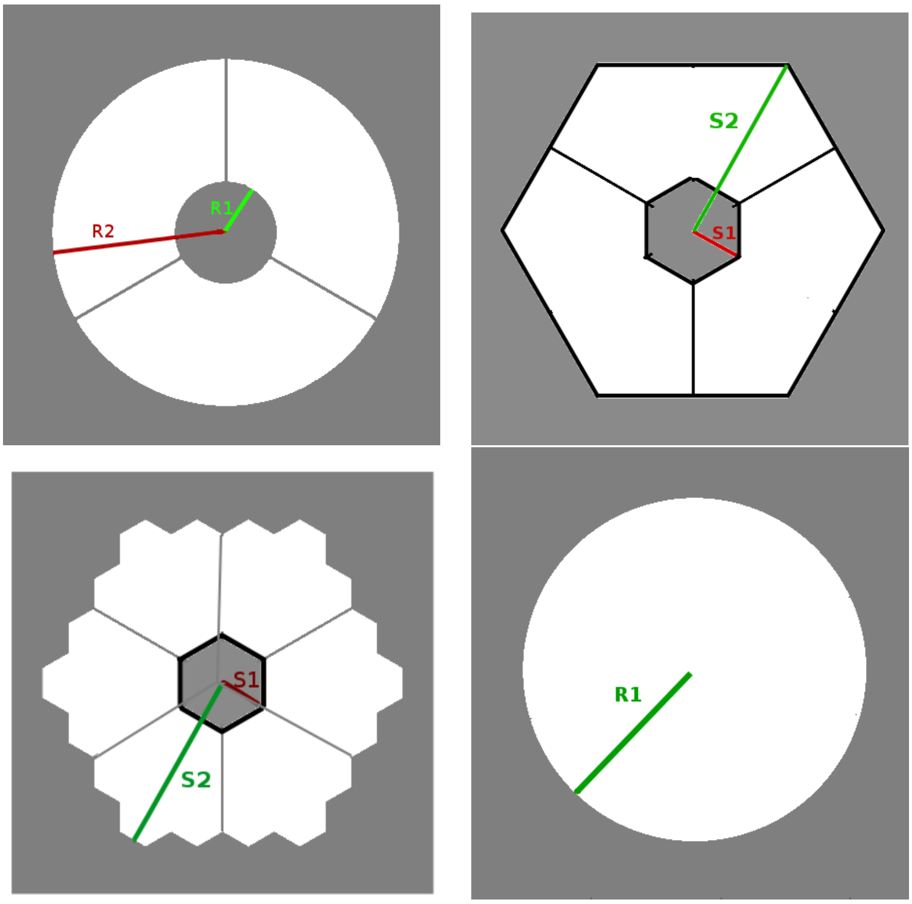

Figure 4.7: Reference radius locations for measurements listed in Table 4.2

Geometry	Wavelength	R_1 (mm)	R_2 (mm)
Annular	Long	1.6114	5.7461
	Short	1.5135	5.7461
Hexagonal	Long	1.7991	6.4363
	Short	1.6668	6.4128
Matched	Long	1.6114	5.7461
	Short	1.5135	5.7461
Open	Long		6.8155

Table 4.2: Radii of inner and outer portions of the masks.

4.3.1 Gain

The gain of a detector is the conversion between measured electrons and ADU. Using the standard voltage settings, the reported Teledyne gain is 2.15 e^-/ADU. In order to verify this gain, we used the photon transfer method (McLean, 2008). This method takes advantage of the Poissonian distribution of incoming photons. Assuming Poissonian statistics, the number of electrons is related to its variance by

$$\sigma_e^2 = N_e \tag{4.1}$$

where σ_e is the standard deviation of the distribution and N_e is the number of incoming electrons. In the Poisson-noise dominated regime

$$N_D = \frac{1}{g} N_e, \tag{4.2}$$

were N_D is the number of ADU and g is the gain in e^-/ADU. Similarly

$$\sigma_D^2 = \frac{\sigma_e^2}{g^2}. \tag{4.3}$$

Therefore

$$g^2 \sigma_D^2 = g N_D \tag{4.4}$$

$$V = \frac{1}{g} N_D \tag{4.5}$$

where V is the variance of ADU.

4.3.1.1 Data and analysis

In order to measure the gain and variance we used the photon transfer curve method. We took thirty images at nine different lamp light levels. We used the open pupil mask to uniformly illuminate the detector with an *Hbb* filter to adjust the received flux to an acceptable range. We took the images in Multiple Correlated Double Sampling (MCDS) mode. For each stack of images at each lamp brightness, we calculated the per-pixel median and variance through the stack. We selected a 500×500 pixel patch that is uniformly illuminated such that the median map is fairly constant. We then found the medians of the median and variance maps

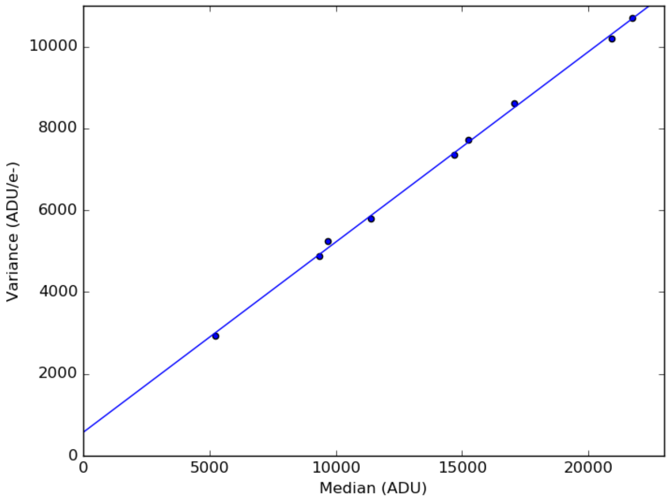

Figure 4.8: The median of the median and variance maps at each lamp brightness. The inverse of the slope of the fitted line implies a gain of 2.16 ± 0.34.

for each brightness. We plot these medians in Figure 4.8 and fit a line through the data. The inverse of the slope of this line gives a gain of 2.16 ± 0.34, in good agreement with the quoted Teledyne gain of 2.15.

There are other methods to calculate the median and variance of any given illumination that were not selected. One method is to calculate the per-pixel median and variance at each brightness to find a per-pixel gain. This method was not selected as thirty images was too few to get a tight distribution on the gains. This led to much larger error bars than taking representative values (medians) of the per-pixel medians and variances. Another method is to increase the amount of illumination by increasing the integration time. However, the read noise is not constant with integration time which would result in non-linearity in the median vs variance curve, whereas keeping the integration time constant makes the read noise a constant shift.

4.3.2 Read noise

We measured the read noise by taking a series of images in MCDS mode. In this mode a series of reads (a group) is taken at the beginning of the exposure and another series at the end. The final image is the difference of the mean of the two groups. Increasing the number of reads decreases the read noise, though it the maximum number of reads is limited by the integration time, as the minimum read time for an H2-RG detector is 1.476 seconds (at 100 kHz pixel clock). In Table 4.3, we list the read noise for various integration times using the maximum number of reads.

Table 4.3: Read noise for varying numbers of reads and integration times for MCDS exposures.

Integration time (s)	Number of reads per group	Read noise (e^-)
1.476	1	23.4 ± 1.3
2.951	2	13.7 ± 1.0
4.427	3	11.6 ± 0.8
5.902	4	9.9 ± 0.8
7.477	5	9.0 ± 0.7
8.852	6	8.4 ± 0.6
10.328	7	7.7 ± 0.4
11.804	8	7.6 ± 0.3
23.605	16	5.6 ± 0.3
47.210	32	5.0 ± 0.2
94.418	64	4.7 ± 0.1

Table 4.4: Linearity characteristics

Deviation at the 1% level	44,500 e^-
Deviation at the 5% level	80,000 e^-
Maximum well capacity	119,000 e^-

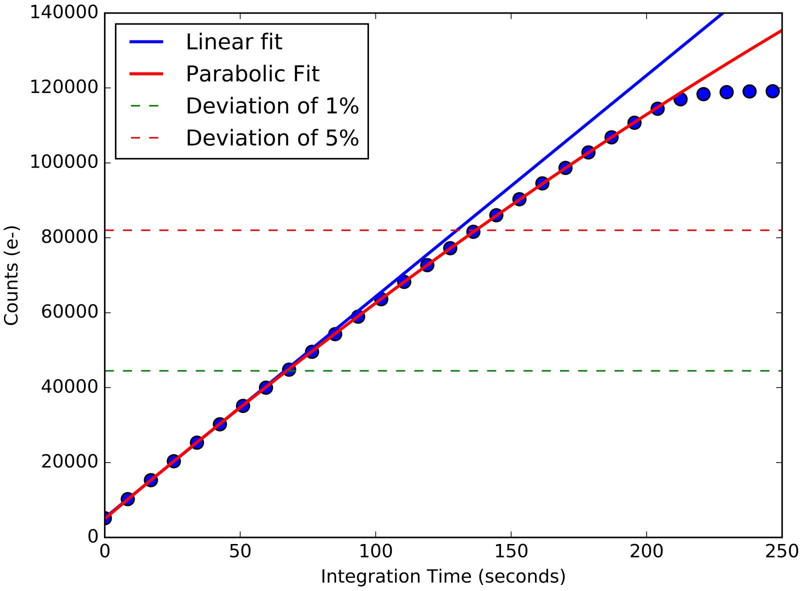

Figure 4.9: Median counts as a function of integration time with a constant lamp brightness. A linear fit to the lower data points is shown in blue while a parabolic fit to the upper data points is shown in red.

4.3.3 Dark current

Infrared detectors exhibit dark current as a result of the thermal energy of electrons. To mitigate this effect, we hold the detector at a constant temperature of 70 K. We measured the remaining dark current using ten up-the-ramp (UTR) exposures, in which reads are taken at regular intervals along the exposure. We wrote out each read and calculated the median number of counts as a function of time. At each integration time we took the average of the ten exposures and plot them in Figure 4.10. The slope of the fitted line implies an upper limit on the dark current of <0.021 e^{-}/pix/s which is lower then the quoted Teledyne dark current of <0.05 e^{-}/pix/s. This is not expected to be a limiting source of noise for broadband imaging.

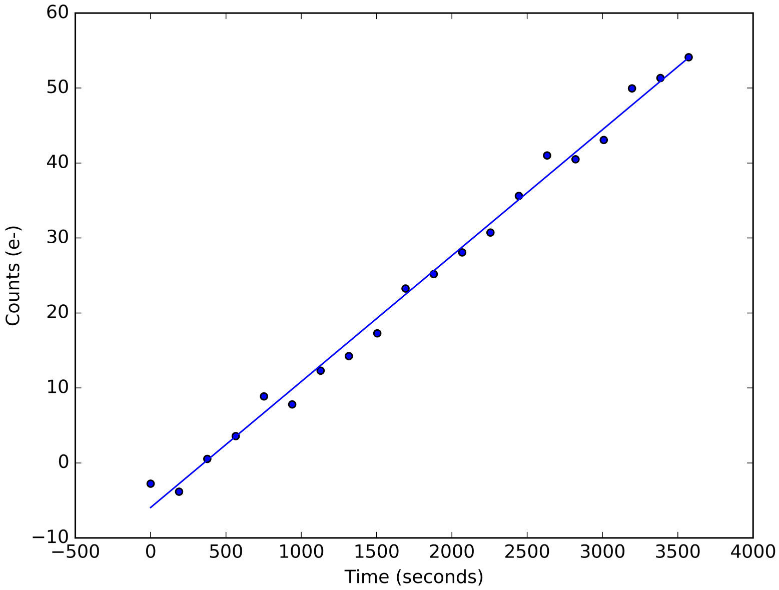

Figure 4.10: Electrons as a function of time in a dark setting. This implies an upper limit on the dark current of <.021 e^-/pix/s

4.3.4 Linearity

Infrared detectors have a non-linear relation between the photon flux and output ADU at high fluxes. In order to characterize this non-linearity, we took a series of images increasing in integration time until saturation. We fitted a line to the linear region of the counts vs. time and a parabola to the non-linear region as shown in Figure 4.9. We then took the difference of the two curves to calculate the deviation from linearity. We show characteristic values in Table 4.4.

Bibliography

Bell, C. P. M., Mamajek, E. E., & Naylor, T. 2015, A self-consistent, absolute isochronal age scale for young moving groups in the solar neighbourhood, arXiv:1508.05955

Beuzit, J. L., Vigan, A., Mouillet, D., et al. 2019, ApJ, arXiv:1902.04080

Bohren, C. F., & Huffman, D. R. 2009, Absorption and scattering of light by small particles (Wiley-VCH)

Bowler, B. P., & Nielsen, E. L. 2018, ArXiv e-prints, arXiv:1802.10132

Chen, C. H., Mittal, T., Kuchner, M., et al. 2014, ApJS, 211, 25

Esposito, T. M., Kalas, P., Fitzgerald, M. P., et al. 2020, arXiv e-prints, arXiv:2004.13722

Foreman-Mackey, D., Hogg, D. W., Lang, D., & Goodman, J. 2013, PASP, 125, 306

Gaia Collaboration, Prusti, T., de Bruijne, J. H. J., et al. 2016, A&A, 595, A1

Greaves, J. S., Mannings, V., & Holland, W. S. 2000, Icarus, 143, 155

Hinkley, S., Oppenheimer, B. R., Soummer, R., et al. 2009, ApJ, 701, 804

Hughes, A. M., Duchêne, G., & Matthews, B. C. 2018, ARA&A, 56, 541

Jura, M. 1991, ApJ, 383, L79

Khare, B. N., Sagan, C., Arakawa, E. T., et al. 1984, Icarus, 60, 127

Koerner, D. W., Ressler, M. E., Werner, M. W., & Backman, D. E. 1998, ApJ, 503, L83

Konopacky, Q. M., Thomas, S. J., Macintosh, B. A., et al. 2014, in Society of Photo-Optical Instrumentation Engineers (SPIE) Conference Series, Vol. 9147, Ground-based and Airborne Instrumentation for Astronomy V, 914784

Lagrange, A.-M., Bonnefoy, M., Chauvin, G., et al. 2010, Science, 329, 57

Larkin, J., Barczys, M., Krabbe, A., et al. 2006, in Proc. SPIE, Vol. 6269, Society of Photo-Optical Instrumentation Engineers (SPIE) Conference Series, 62691A

Li, A., & Draine, B. T. 2001, ApJ, 554, 778

Li, A., & Greenberg, J. M. 1997, A&A, 323, 566

—. 1998, A&A, 331, 291

Li, A., & Lunine, J. I. 2003, ApJ, 590, 368

Lisse, C. M., Sitko, M. L., Marengo, M., et al. 2017, AJ, 154, 182

Macintosh, B., Graham, J., Palmer, D., et al. 2006, in Society of Photo-Optical Instrumentation Engineers (SPIE) Conference Series, Vol. 6272, 62720L

Mannel, T., Bentley, M. S., Schmied, R., et al. 2016, MNRAS, 462, S304

Marois, C., Lafrenière, D., Doyon, R., Macintosh, B., & Nadeau, D. 2006, ApJ, 641, 556

Mathis, J. S., Rumpl, W., & Nordsieck, K. H. 1977, ApJ, 217, 425

Mayor, M., & Queloz, D. 1995, Nature, 378, 355

McLean, I. S. 2008, Electronic Imaging in Astronomy (NewChichester, UK: Praxis)

Milli, J., Vigan, A., Mouillet, D., et al. 2017, A&A, 599, A108

Milli, J., Engler, N., Schmid, H. M., et al. 2019, arXiv e-prints, arXiv:1905.03603

Min, M., Hovenier, J. W., & de Koter, A. 2005, A&A, 432, 909

Nesvold, E. R., & Kuchner, M. J. 2015, ApJ, 798, 83

Olofsson, J., Milli, J., Thébault, P., et al. 2019, A&A, 630, A142

Perrin, M. D., Maire, J., Ingraham, P., et al. 2014, in Proc. SPIE, Vol. 9147, Ground-based and Airborne Instrumentation for Astronomy V, 91473J

Perrin, M. D., Duchene, G., Millar-Blanchaer, M., et al. 2015, ApJ, 799, 182

Pinte, C., Ménard, F., Duchêne, G., & Bastien, P. 2006a, A&A, 459, 797

—. 2006b, A&A, 459, 797

Pollack, J. B., Hollenbach, D., Beckwith, S., et al. 1994, ApJ, 421, 615

Pueyo, L. 2016, ApJ, 824, 117

Quillen, A. C. 2006a, MNRAS, 372, L14

—. 2006b, MNRAS, 372, L14

Rodigas, T. J., Stark, C. C., Weinberger, A., et al. 2015, ApJ, 798, 96

Schneider, G., Weinberger, A. J., Becklin, E. E., Debes, J. H., & Smith, B. A. 2009, AJ, 137, 53

Schneider, G., Smith, B. A., Becklin, E. E., et al. 1999, ApJ, 513, L127

Schneider, G., Grady, C. A., Hines, D. C., et al. 2014, AJ, 148, 59

Sheret, I., Dent, W. R. F., & Wyatt, M. C. 2004, MNRAS, 348, 1282

Soummer, R., Pueyo, L., & Larkin, J. 2012, ApJ, 755, L28

van Leeuwen, F. 2007, A&A, 474, 653

Wang, J. J., Ruffio, J.-B., De Rosa, R. J., et al. 2015, pyKLIP: PSF Subtraction for Exoplanets and Disks, Astrophysics Source Code Library, ascl:1506.001

Wang, J. J., Rajan, A., Graham, J. R., et al. 2014, in Proc. SPIE, Vol. 9147, Ground-based and Airborne Instrumentation for Astronomy V, 914755

Wyatt, M. C. 2008, ARA&A, 46, 339

Wyatt, M. C., Dermott, S. F., Telesco, C. M., et al. 1999, ApJ, 527, 918

Zubko, V. G., Mennella, V., Colangeli, L., & Bussoletti, E. 1996, MNRAS, 282, 1321